Article

Not peer-reviewed version

Functionalized Magnetic Fe_3O_4 Nanoparticles for Targeted Methotrexate Delivery in Ovarian Cancer Therapy

Julia Nowak-Jary * , Artur Płóciennik , Beata Machnicka

Posted Date: 1 July 2024

doi: 10.20944/preprints202407.0042.v1

Keywords: magnetic iron oxide nanoparticles; methotrexate; ovarian cancer; cytotoxicity

Preprints.org (www.preprints.org) | NOT PEER-REVIEWED | Posted: 1 July 2024 doi:10.20944/preprints202407.0042.v1

Article

Functionalized Magnetic Fe_3O_4 Nanoparticles for Targeted Methotrexate Delivery in Ovarian Cancer Therapy

Julia Nowak-Jary [1],*, Artur Płóciennik [2] and Beata Machnicka [1]

[1] Department of Biotechnology, Institute of Biological Sciences, University of Zielona Gora, Prof. Z. Szafrana 1, 65-516 Zielona Gora, Poland
[2] Institute of Experimental Biology, University of Poznan, Uniwersytetu Poznańskiego 6, 61-614 Poznan, Poland
* Correspondence: J.Nowak-Jary@wnb.uz.zgora.pl

Abstract: Magnetic Fe_3O_4 nanoparticles (MNPs) functionalized with (3-aminopropylo)trietoksysilan (APTES) or N-carboxymethylchitosan (CMC) were proposed as nanocarriers of methotrexate (MTX) against ovarian cancer cell lines. The successful functionalization of the obtained nanostructures was confirmed by FT-IR spectroscopy. Nanopnrticles were characterized by transmission electron spectroscopy (TEM) and dynamic light scattering (DLS) techniques. Their potential zeta, magnetization, and hyperthermic properties were also explored. MTX was conjugated with nanocarriers by ionic bonds or by amide bonds. For all three types of nanostructures, the drug release kinetics were examined at different pH and temperatures. The MTT assay showed no toxicity of MNPs[APTES] and MNPs[CMC]. Finally, the cytotoxicity of the nanostructures with MTX attached was measured towards the ovarian cancer cells model sensitivity and resistance to methotrexate in simplistic 2D and spheroid 3D conditions. The results of cytotoxicity tests of the tested nanostructures showed similar values for inhibiting the proliferation of ovarian cancer cells as methotrexate in its free form. Conjugating MTX with nanoparticles allows the drug to be directed to the target site using an external magnetic field, reducing overall toxicity. Combining this approach with hyperthermia could enhance the therapeutic effect in vivo compared to free MTX, though further research on advanced 3D models is needed.

Keywords: magnetic iron oxide nanoparticles; methotrexate; ovarian cancer; cytotoxicity

---

1. Introduction

Due to advances in nanotechnology, magnetic iron oxide nanoparticles (MNPs) (magnetite Fe_3O_4) are now being extensively used for medicine. The uniqueness of MNPs comes from their ferromagnetic nature as they consist of areas of permanent magnetization (so-called magnetic domains), generating a magnetic field around them (like small magnets). Because of their magnetism, simple synthesis and functionalization, large specific surface area, biocompatibility, biodistribution, and physicochemical properties, MNPs are employed in i.e., tumors imaging (MRI) [1–3], radiolabelling and internal radiotherapy [4], hyperthermia [5,6], gene therapy [7], drug delivery and theranostic [8,9]. Especially, magnetic nanoparticles have been considered feasible candidates for developing novel antitumor therapeutics with the potential to overcome drug resistance of cancer cells.

According to statistical data, resistance to cytotoxic drugs is responsible for 90% of deaths due to cancer [10]. The heterogeneity and mutations among cancer cells allow them to develop multidrug resistance (MDR) mechanisms, which increase their chances of survival in the presence of cytotoxic drugs. These mechanisms result in reduced drug influx, increased drug excretion, drug metabolism, and DNA repair, lack of apoptotic mechanisms, and increased activity of anti-apoptotic mechanisms.

The mechanisms of multidrug resistance can be divided into mechanisms at the cellular level and mechanisms specific to cancer tissue [11]. Membrane proteins from the ABC transporter family (ATP-binding cassette), such as P-glycoprotein (MDR1, ABCB1) or breast cancer resistance protein (BCRP), multidrug resistance protein 1 (MRP1, ABCC1)) (multidrug resistance-associated protein 1) are responsible for regulating the distribution, absorption, and excretion of various chemicals [10,12]. Overexpression of these transporters in cancer cells leads to the reduced intracellular concentration of cytostatics [13]. For example, the overproduction of BCRP and MRP1 proteins has been associated with methotrexate resistance [14]. The main role of many cytostatics, such as methotrexate, is to inhibit key enzymes, e.g., dihydrofolate reductase involved in controlling cell proliferation. Cancer cells in approximately 10% of all cancers can amplify the gene encoding the desired enzyme and thus produce more of this enzyme and inhibit inhibition [15].

Moreover, cancers are closely associated with the surrounding microenvironment including blood vessels, lymphatic vessels, stromal cells, and the extracellular matrix [16]. The tumor microenvironment may lead to its resistance to cytostatics through physical and biological barriers [17]. Avoiding the delivery of drugs to the tumor is facilitated by the atypical blood and lymphatic vasculature of the tumor. Heterogeneously distributed tumor blood vessels, formed in the process of angiogenesis, generate areas with low oxygen concentration. Hypoxic areas play a key role in cytostatic resistance because: they inhibit the profiling of cancer cells and make them resistant to active drugs; drugs are not typically delivered to hypoxic areas at toxic concentrations; hypoxia regulates genes related to drug resistance and export via the P-glycoprotein pump [18]. Moreover, hypoxia induces specific cancer cell signaling pathways such as NFκB, MAPK, PI3K, and HIF, generating negative and positive feedback loops [19]. Atypical tumor vessels also result in the formation of acidic pH in the extracellular matrix, which affects the localization and release of cytostatics [17]. The lymphatic system is changed in the tumor environment. Abnormalities in the functioning of lymphatic vessels, such as improper permeability, result in a weakened immune response and increased drug resistance [20]. Furthermore, immune cells such as cancer-associated fibroblasts (CAF), tumor-associated neutrophils (TAN), and tumor-associated macrophages (TAM) mediate drug resistance using various mechanisms, such as physical contact with tumor-infiltrating immune cells and drug molecules or the production of cytokines and chemokines that block the activation of regulatory T cells (Tregs) [21]. The extracellular space of most solid tumors has a matrix rich in collagen, which creates a dense network that prevents uniform drug delivery to the tumor. Therefore, drug delivery to the tumor largely depends on the volume fraction of the components (in particular collagen and proteoglycan) and the organization of the extracellular matrix [17]. As a result of the interaction of cells with the tumor matrix through activated β1 integrin, the tumor acquires drug resistance associated with loss of cell adhesion (CAM-DR) (cell adhesion mediated drug resistance). This phenomenon has been observed in ovarian cancer, glioma, leukemia, and lung cancer [22]. In addition, multidrug resistance is directly affected by the presence of cancer stem cells (CSCs) in the tumor. CSCs are characterized by the ability to self-renew and differentiate into various cancer cell lines, they can: be in a quiescent state (free from cell division), show increased expression of drug resistance proteins, and can be active in the regulation of signaling pathways [11,23].

Some of the above-mentioned phenomena specific to cancer tumors in vivo conditions can be observed in three-dimensional cell models [24]. Although the advantages of 2D monolayer culture are their simple and cheap maintenance and the ease of performing functional tests, cells growing in 2D culture do not imitate the natural structures of tissues or tumors. In this culture method, cell-cell and cell-environment interactions are not represented as in the tumor environment. These interactions are responsible for cell differentiation, proliferation, viability, gene and protein expression, response to stimuli, and cellular metabolism [25]. Adherently growing cells lose their polarity, which changes the response of these cells to various phenomena, e.g., apoptosis [26]. In an adherent monolayer culture, cells benefit from unlimited access to media components such as oxygen, nutrients, metabolites, and signaling molecules. However, in the case of cancer cells that form tumors, the variability in access to nutrients results mainly from their specific structure, which cannot be reflected by cell culture in 2D conditions [25,27]. It has also been observed that culture in

2D conditions changes gene expression and splicing, cell topology, and biochemistry [25,28,29]. The concept of culturing cancer cells in 3D is based on the creation of spheroidal structures that mimic the physical and biochemical aspects of the tumor mass. In this cellular model, there are intercellular and cell-environment interactions similar to those that occur in vivo [30,31]. The natural morphology, polarity, cell topology, gene expression, signaling, and metabolism, there is more similar to in vivo conditions [32]. All these features of the cell model in three-dimensional culture make it widely used to study the biology of cancer cells, invasion, and metastasis processes, as well as for testing drugs and new therapies.

To attempt to overcome the drug resistance to methotrexate in ovarian cancer cells, we designed nanoparticles with the drug attached. First, Fe_3O_4 nanoparticles functionalized with APTES or CMC were synthesized. The proper coating of the Fe_3O_4 core increases the biocompatibility of magnetic nanocarriers and reduces their potential toxicity. The polymer shell minimizes free iron ions release, which is believed to participate in the Haber-Weiss, Fenton, and Fenton-like reactions being one of the main processes generating reactive oxygen species (ROS) such as superoxide anions, hydroxyl radicals, and hydrogen peroxides [33]. Additionally, coating molecules can provide various functional groups serving as linkers for therapeutic attaching. As an example, aminosilanes, including 3-(aminopropyl)triethoxysialne (APTES) [34,35], are frequently used for MNPs functionalization since they afford amine groups for drug binding. Other often applied biocompatible polymers are chitosan and its derivatives such as N-carboxymethylchitosan (CMC) equipped with carboxyl groups [36]. These molecules are also responsible for the resultant MNPs charge, influencing their stability in the media.

Obtained Fe_3O_4 nanoparticles functionalized with APTES or CMC were confirmed by FT-IR spectra. Next, MNPs were characterized using TEM imaging, DLS, and zeta potential measurements. Magnetic and hyperthermic properties of the nanostructures were also investigated. To the MNPs[APTES] and MNPs[CMC], methotrexate finally was attached, and the cytotoxicity of the obtained nanostructures towards the ovarian cancer cells model was measured in simplistic 2D as well as spheroid 3D conditions.

2. Results

2.1. Characterization with FT-IR and Transmission Electron Microscope (TEM) Imaging of APTES- and CMC-Modified Nanoparticles (MNPs[APTES] and MNPs[CMC])

The TEM images (Figure 1) show that the MNPs[APTES] and MNPs[CMC] have a uniform shape and size distribution with a diameter of approximately 10 nm. The effect of the surface functionalization of the MNPs with APTES and CMC, respectively, was confirmed by FT-IR spectrum in the range of 4000–400 cm^{-1} (Figure 2 a, b). The intensive absorption band at 585 cm^{-1} for MNPs[APTES] sample is associated with the metal-oxygen Fe–O bonds in the crystalline lattice of Fe_3O_4 (stretching vibrations). The broadband centered at 3431 cm^{-1} derives from N-H stretching vibrations of APTES. The absorption bands at 2922 cm^{-1} and 2850 cm^{-1} correspond to carbon aliphatic chains C–H (stretching vibrations), whereas these between 1650-1560 derive from N-H deformation vibrations. The band at 1081 cm^{-1} comes from C-N stretching vibrations and overlaps with Si–O asymmetry stretching vibrations, whereas the bands at 875 and 794 cm^{-1} correspond to Si-O symmetry stretching vibrations. The absorption band at 585 cm^{-1} in the case of MNPs[CMC] sample corresponds to the Fe–O bonds in the crystalline lattice of Fe_3O_4 (stretching vibrations). The broad band at 3446 cm^{-1} derives from stretching vibrations of N-H and O-H bonds, whereas the bands at 2917 and 2850 cm^{-1} are attributed to the C-H stretching vibration bonds. The spectrum bands at 1654 and 1560 cm^{-1} represent deformation vibrations of N-H, in turn at 1074 cm^{-1} stretching vibrations of C-N. The band at 1419 cm^{-1} displays symmetrical stretching vibrations of O-H (COOH), whereas the band at 1701 cm^{-1} stretching vibrations of C=O (COOH). As observed, the spectra of MNPs[APTES] and MNPs[CMC] are very similar due to the presence of many of the same types of bonds.

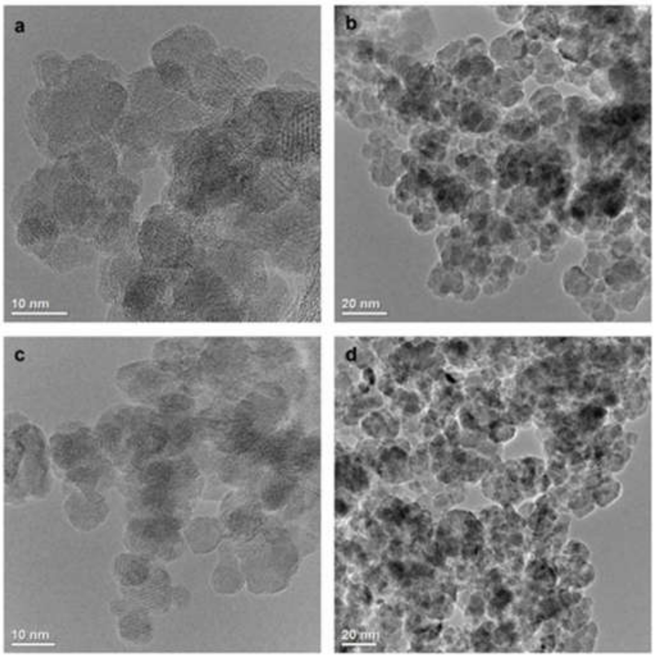

Figure 1. TEM images of MNPs[APTES] (a, b) and MNPs[CMC] (c, d).

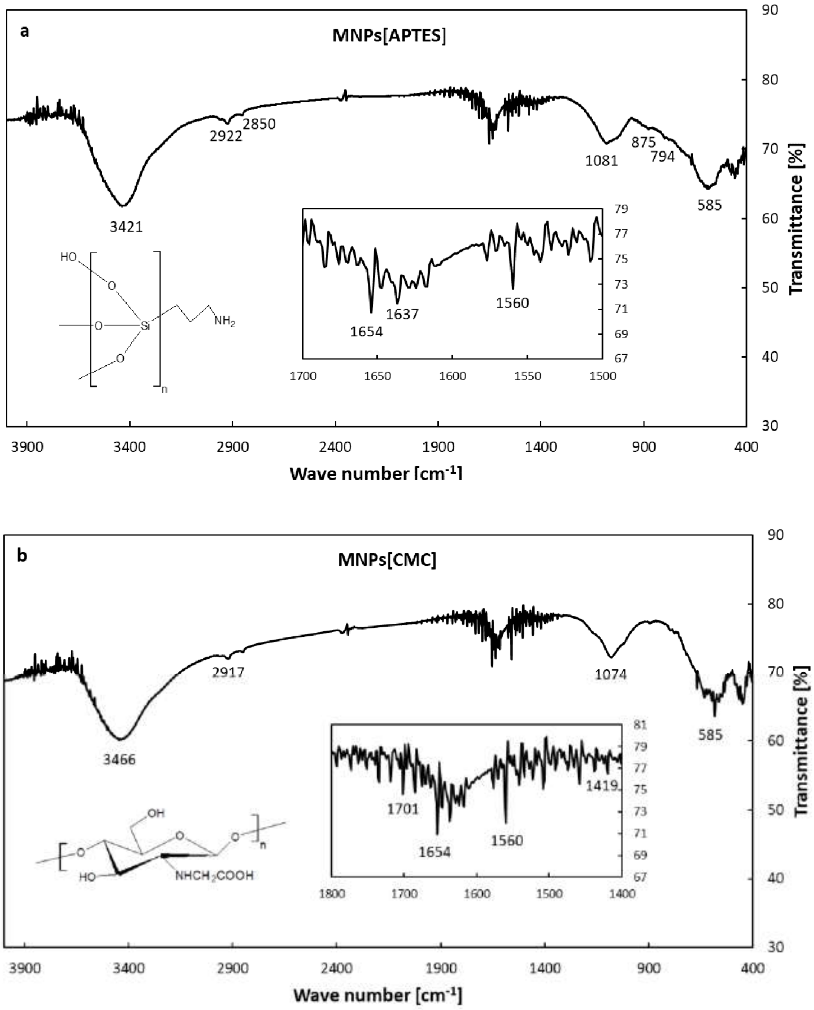

Figure 2. FT-IR spectra of MNPs[APTES](a) and MNPs[CMC] (b).

2.2. Magnetic VSM Properties Measurements of MNPs[APTES] and MNPs[CMC]

The results obtained for MvT measurements are shown in Figure 3. In the case of both samples, they indicate a superparamagnetic nature with a blocking temperature (T_B) estimated from the point inflections of the dM/dT curve at 103 K for MNPs[CMC] and 113 K for MNPs[APTES] nanoparticles. Comparison of the shape of the measured loops and field relationships coercivity (H_C), magnetization saturation (M_S), and magnetic remanence (M_R) as a function of temperature are presented in Figure 4. The M_S(T) relationship is typical for ferrimagnetic iron oxide spinel structure. The nature of the H_C(T) and M_R(T) relationships are akin to each other, which suggests that the dominant source of magnetic hysteresis is the blocking effect of single-domain particles when energy volume anisotropy is higher than the energy of thermal excitations.

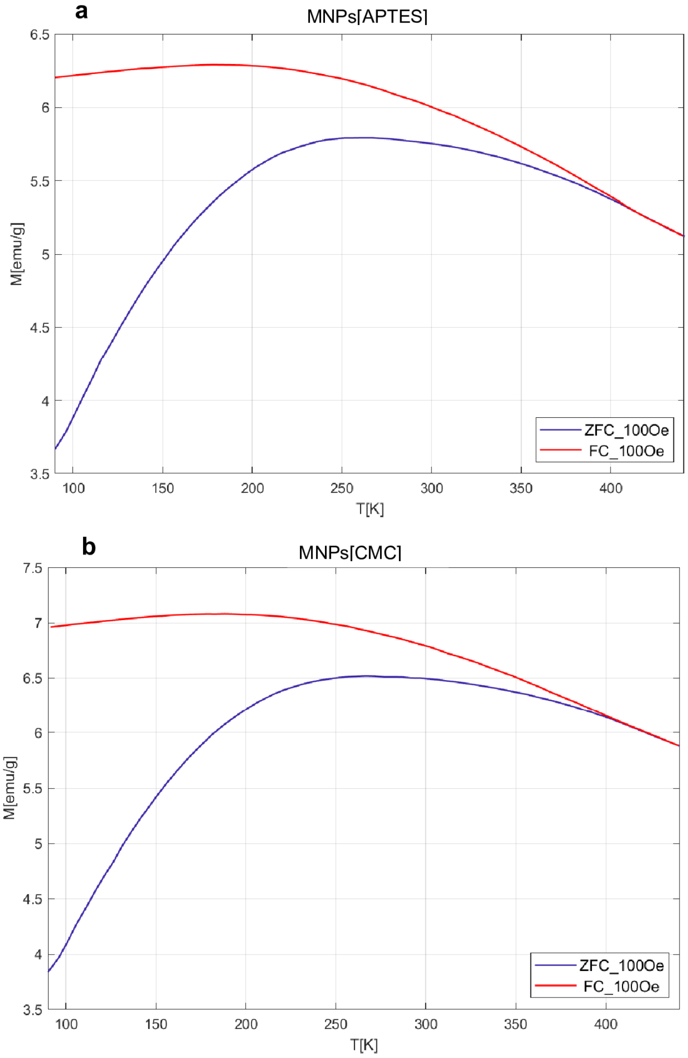

Figure 3. M(T) relationships of the ZFC and FC type for the APTES sample (a) and CMC (b).

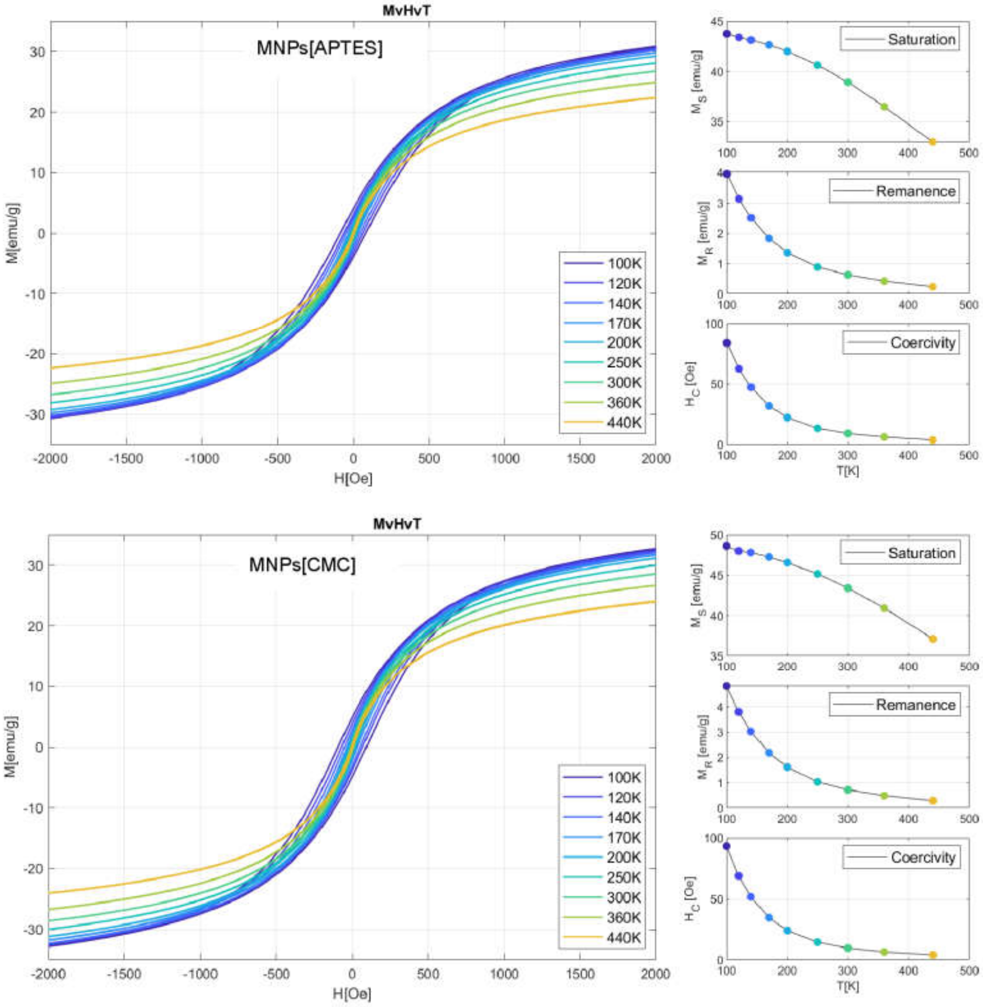

Figure 4. M(H) dependencies for nine selected temperatures in the range from 100 K to 440 K and determination on their basis magnetization saturation, remanence, and coercivity field. The results for the MNPs[APTES] sample are presented in the upper panel and for the MNPs[CMC] sample in the lower panel.

2.3. Hyperthermic Properties of MNPs[APTES] and MNPs[CMC]

The temperature increases as a function of time generated by nanoparticles under the influence of an external electromagnetic field at given current intensities, as shown in Figure 5. The results indicate significant hyperthermal properties of the tested nanostructures, whereby for MNPs[CMC] they are stronger than for MNPs[APTES]. For example, at a current of 250 A, MNPs[APTES] generate a temperature increase to 45°C after about 370 seconds, while MNPs[CMC] raise the temperature to the same value after about 120 seconds.

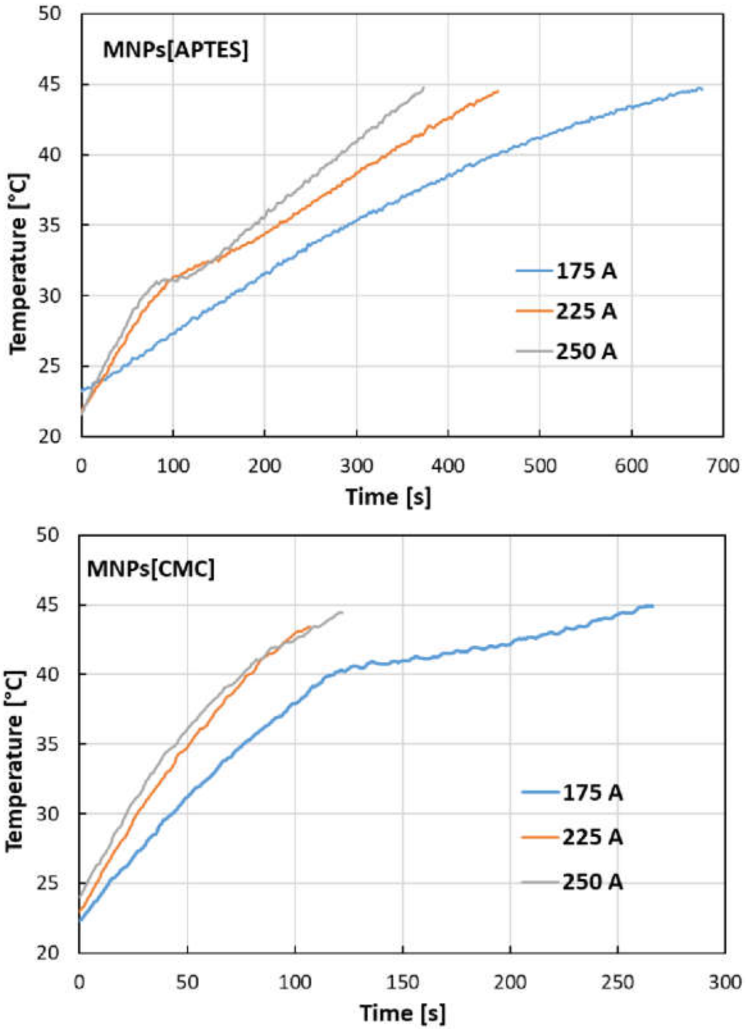

Figure 5. Dependencies of temperature on heating time for MNPS[APTES] and MNPs[CMC] samples for different current values (frequency of magnetic field approx. 360 MHz).

Based on the measurements performed using magnetic hyperthermia equipment, the SAR (specific absorption rate) and ILP (intrinsic loss) parameters [37–39] were determined and summarized in Table 1. SAR quantifies the ability of magnetic nanoparticles to absorb energy from an alternating magnetic field and can be described by the equation:

$$SAR = C \times \frac{\mathrm{d}T}{\mathrm{t}t} \times \frac{1}{m_{Fe}} \qquad [\mathrm{W/g}]$$

where: C is the heat capacity of the medium (for water C = 4.189 J/g · K), T—temperature [K], t—time [s], m_{Fe}—mass of iron in the sample. dT/dt element is determined by fitting a straight line to the initial rectilinear fragment of the temperature vs. time on the graph and reading the slope coefficient of this line. The ILP parameter considers additionally the intensity and frequency of the magnetic field. Its value is calculated using the equation:

$$ILP = \frac{SAR}{f \times H^2} \qquad [\mathrm{nHm^2/kg}]$$

where: H – magnetic field intensity, f – magnetic field frequency.

SAR and ILP values for induction heating of MNPs[APTES] nanoparticles in an alternating magnetic field increased with the increase in the electromagnetic field intensity (175, 225, and 250 A). In the case of inductive heating MNPs[CMC] nanoparticles in an alternating magnetic field, the SAR parameter value also increased with the increase of the electromagnetic field strength, however the determined SAR and ILP values for MNPs[CMC] were several times higher compared to the values determined for MNPs[APTES] nanoparticles.

Table 1. Summary of SAR and ILP parameters results.

Aqueous solution of MNPs[APTES] nanoparticles, C = 4 mg MNPs/ml					
I = 175 A		**I = 225 A**		**I = 250 A**	
H [kA/m]	**27.64**	H [kA/m]	**33.83**	H [kA/m]	**36.41**
f [kHz]	**356**	f [kHz]	**357**	f [kHz]	**356**
SAR (W/g)	**59**	SAR (W/g)	**114**	SAR (W/g)	**154**
H [kA/m]	**0.22**	ILP [nH^2/kg]	**0.28**	ILP [nH^2/kg]	**0.33**
Aqueous solution of MNPs[CMC] nanoparticles, C = 4 mg MNPs/ml					
SAR (W/g)		**I = 225 A**		**I = 250 A**	
ILP [nH^2/kg]	**27.64**	H [kA/m]	**33.83**	H [kA/m]	**36.41**
f [kHz]	**356**	f [kHz]	**357**	f [kHz]	**356**
SAR (W/g)	**208**	SAR (W/g)	**314**	SAR (W/g)	**364**
ILP [nH^2/kg]	**0.76**	ILP [nH^2/kg]	**0.77**	ILP [nH^2/kg]	**0.77**

2.4. Capability of MTX Loading

Schemes of methods for attaching MTX to magnetic nanoparticles functionalized with APTES and CMC are illustrated in Figure 6.

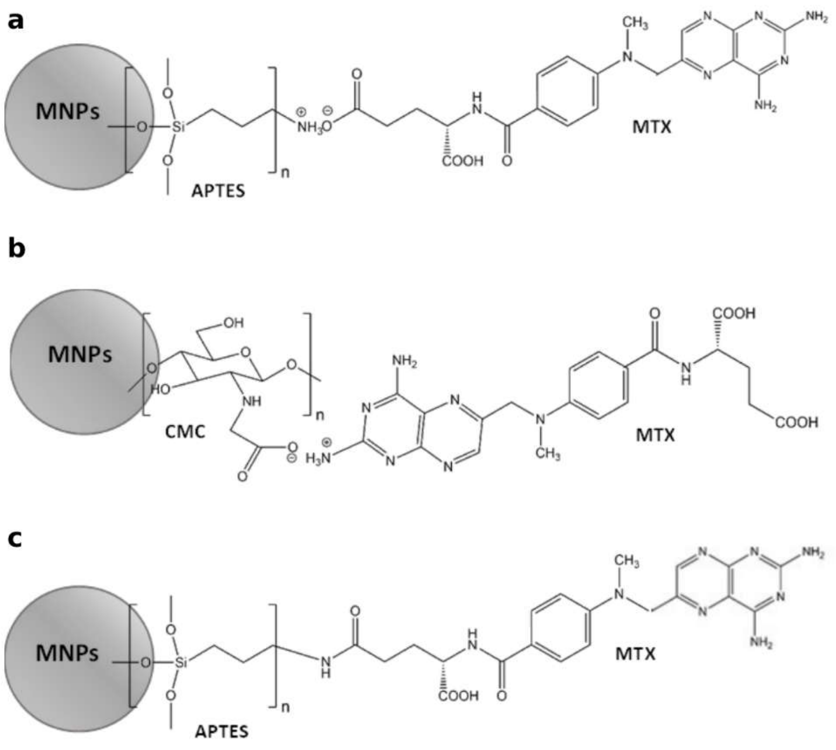

Figure 6. Methods for attaching of MTX on MNPs[APTES] – ionic bond (a), MNPs[CMC] – ionic bond (b), MNPs[APTES] – amide bond (c).

Considering that 30 mg of MTX were added to 600 mg of MNPs[APTES] (ionic bond) or MNPs[CMC] (Experimental part), 100% efficiency of loading was theoretically 50 µg MTX per 1 mg of MNPs[APTES]MTX or MNPs[CMC]MTX, respectively. The results of MTX loading capacity quantitation showed that 1 mg of MNPs[APTES]MTX contained 31 µg of MTX, which gave capability of the drug loading equal to 62%, whereas 1 mg of MNPs[CMC]MTX contained 43.6 µg of MTX, which gave capability of the drug loading equal 87.2%. In the case of MTX conjugated with MNPs[APTES] via an amide bond, the loading efficiency was 18.8 % (9,4 µg MTX per 1 mg of nanoparticles).

2.5. DLS and Zeta Potential Measurements of MNPs[APTES], MNPs[CMC] and MTX-Functionalized Nanoparticles (MNPs[APTES]MTX and MNPs[CMC]MTX)

The functionalization of MNPs with APTES and CMC, and the presence of MTX on the nanoparticles surface was further confirmed with the change of surface charge. ζ-Potential of bare MNPs was -18.8 mV (SD = 0.44). Following the coating with APTES and CMC, the charge of the nanoparticles surface changed to values equal +8.4 mV (SD = 0.39) and -18.9 mV (SD = 1.33), respectively. After conjugation of MTX, nanoparticles exhibited consecutive ζ-Potential values: MNPs[APTES]MTX (ionic bond) -7.4 mV (SD = 0.06), MNPs[CMC]MTX -20.3 mV (SD = 0.74) and MNPs[APTES]MTX (amide bond) -6.1 mV (SD = 0.36). The hydrodynamic diameters (d_H) of nanoparticles were determined by DLS method. The hydrodynamic diameter includes nanoparticles together with all the solvated ions of the environment in which the nanoparticles are suspended; therefore, its value is usually much larger than that determined by electron microscopy such as TEM [40]. The obtained D_H values in the buffer with a composition corresponding to the RPMI 1640 medium were as follows: bare MNPs ~ 90 nm, MNPs[APTES] ~ 260 nm, MNPs[CMC] ~ 36 nm, MNPs[APTES]MTX (ionic bond) ~ 150 nm, MNPs[CMC]MTX ~ 240 nm, MNPs[APTES]MTX (amide bond) ~ 220 nm. Considering quite high polydispersity indexes (a measure of the heterogeneity of a sample based on size) ranging from 0.3 to 0.4, it can be assumed that the large hydrodynamic diameters could also result from a certain degree of nanoparticle agglomeration.

2.6. Investigation of MTX Release from MNPs[APTES]MTX and MNPs[CMC]MTX (Ionic Bond)

The release rate of MTX immobilized on MNPs[APTES] by ionic bonds is shown in Figure 7 a, b as the percentage increase of the drug in solution, where the total amount of MTX immobilized on a given number of nanoparticles was considered as 100%. The drug was released from MNPs[APTES] rapidly according to first-order kinetics for all pH and temperature conditions. After 15 minutes at 37°C, approx. 95% (pH=7.5) or 80% (pH=6.0) of the total amount of the drug was released, while at 45°C, approx. 88% of the initial amount of MTX bound on MNPs[APTES] was found in the supernatant for both pH values. In the case of the drug bound with a MNPs[CMC], the MTX release process was much slower and the percentage values of the released drugs at 37°C were as follows: at pH = 7.5 approx. 35% within the first 30 minutes (first order kinetics,) and approx. 50% after next 60 minutes (zero order kinetics starting from the 30th minute of the release); at pH = 6.0 less than 20 % within the first 15 minutes (first order kinetics) and approx. 47% after next 60 minutes (zero order kinetics starting from the 15th minute of the release). The results of the release rate measurements at 45°C were read from the chart (Figure 8 a, b) as follows: at pH = 7.5 approx. 30% released of the total amount of the drug within the first 30 minutes (first order kinetics) and approx. 40 % after next 60 minutes (zero order kinetics starting from the 30th minute of the release); at pH= 6.0 approx. 17% within the first 15 minutes (first order kinetics) and approx. 36% after next 60 minutes (zero order kinetics starting from the 15th minute of the release). In conclusion, the drug release rates for both nanocarriers (MNPs[APTES] and MNPs[CMC], respectively) were lower in a slightly acidic environment (pH = 6.0) and at higher temperature (45°C).

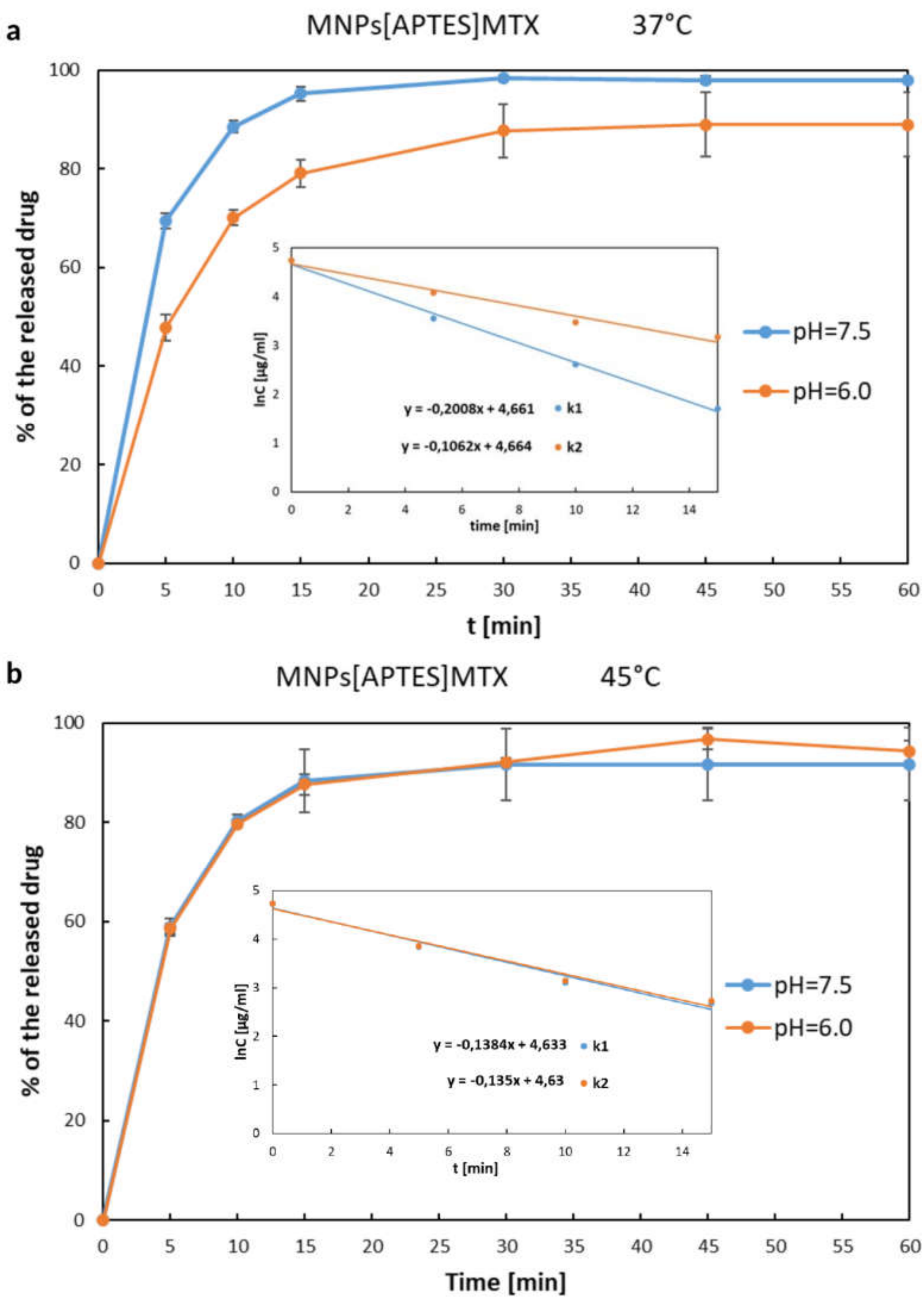

Figure 7. MTX release curves from MNPs[APTES]. Internal graphs present sections corresponding to first-order kinetics, and the slopes indicate the release rate constants: a) k1 - release constant for 37°C, pH=7.5; k2 – release constant for 37°C, pH=6.0; b) k1 - release constant for 45°C, pH=7.5; k2 – release constant for 45°C, pH=6.0.

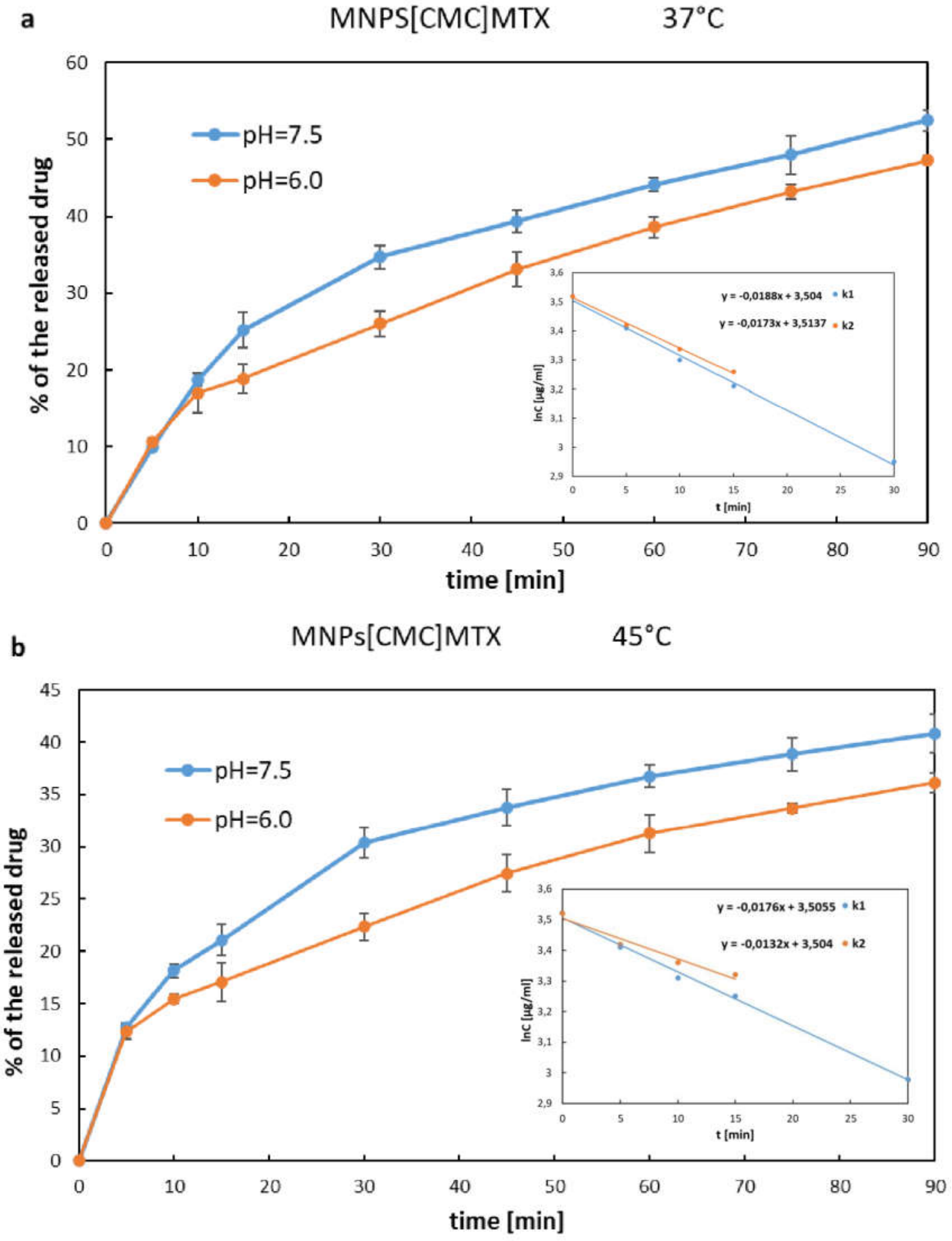

Figure 8. MTX release curves from MNPs[CMC]. Internal graphs present sections corresponding to first-order kinetics, and the slopes indicate the release rate constants: a) k1 - release constant for 37°C, pH=7.5; k2 – release constant for 37°C, pH=6.0; b) k1 - release constant for 45°C, pH=7.5; k2 – release constant for 45°C, pH=6.0.

The release rates were measured as the wastage of the drug from the nanoparticles. Using the equations:

$lnC = -kt + lnC_0$ (first order kinetics) and $C = k_0 \times \Delta t$ (zero order kinetics)

where C_0 – total amount of the immobilized MTX on MNPs[APTES] surface at t = 0 min, the release rate constants were determined and summarized in Table 2.

Table 2. Methotrexate release rate constants.

	MNPs[APTES]MTX			
	37°C		45°C	
	pH = 7.5	pH = 6.0	pH = 7.5	pH = 6.0
0 – 60 min I - order kinetics	k = 0.2008 [min^{-1}]	k = 0.1602 [min^{-1}]	k = 0.1384 [min^{-1}]	k = 0.1350 [min^{-1}]
	MNPs[CMC]MTX			
	37°C		45°C	
	pH = 7.5	pH = 6.0	pH = 7.5	pH = 6.0
0 – 30 min I - order kinetics	k = 0.0188 [min^{-1}]		k = 0.0176 [min^{-1}]	
0 – 15 min I - order kinetics		k = 0.0173 [min^{-1}]		k = 0.0132 [min^{-1}]
30 – 90 min 0 – order kinetics	k_0 = 0.197 [μg/ml×min^{-1}]		k_0 = 0.152 [μg/ml×min^{-1}]	
15 – 90 min 0 – order kinetics		k_0 = 0.176 [μg/ml×min^{-1}]		k_0 = 0.134 [μg/ml×min^{-1}]

2.7. Investigation of MTX Release from MNPs[APTES]MTX (Amide Bond)

The release of MTX bound on nanoparticles via an amide bond was performed at three pH values: 7.5, 6.0, and 2.0, which reflected the environmental conditions of blood serum, tumor intercellular matrix, and intracellular lysosomes, respectively. A common phenomenon in tumors is ion pump disruption [41]. Cancer cells remove H^+ ions to a greater extent than normal cells, which causes an increase in pH inside cells and a decrease in the extracellular matrix. In turn, in intracellular lysosomes, which during normal cellular metabolism are responsible for the breakdown of proteins and other exogenous materials, pH is very low. Following their uptake via receptor-mediated endocytosis, nanoparticles are transported to early endosomes fusing subsequently with lysosomes.

The results of MTX release bound to MNPs[APTES] by amide bond are shown in Figure 9.

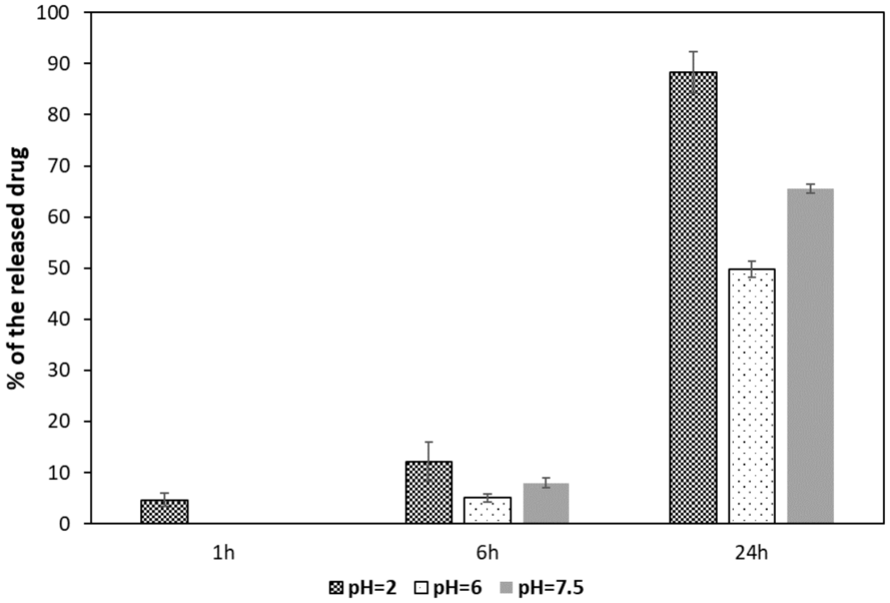

Figure 9. MTX release from MNPs[APTES] (amide bond).

After the first hour of incubation with the enzyme, the degree of hydrolysis of the amide bond was negligible. Only at the lowest pH = 2.0, approximately 5% of the drug was released. After 6 h, the supernatant contained 12% of the total amount of bound methotrexate at pH = 2.0, while at pH =

6.0 and 7.5 approximately 5% and 7%, respectively. After a full day of incubation, almost the entire amount of MTX was released (about 89%) in the environment with the lowest pH, whereas in the supernatant at pH = 6.0, about half of the total bound MTX was found, and 66% at pH = 7.5.

2.8. The Morphology of Cell Model Grown in a 2D and 3D Condition

To check the effect of the obtained forms of cytostatics, in this study, we used the W1 ovarian cancer cell line, derived from the ovarian cancer tissue of an untreated patient, along with the methotrexate-resistant W1MR variant derived from this line. We observed that both kinds of cells grew as a monolayer in the 2D culture method. We could identify epithelial-like cells in W1 and W1MR based on their morphology. These cells were polygonal in dimension and grew attached to a substrate in a coherent colony. Likewise, both cell lines formed spheroids using the 3D culture method. W1 and W1MR cell lines formed similar round-type tightly packed compact spheroids with regular edges (Figure 10).

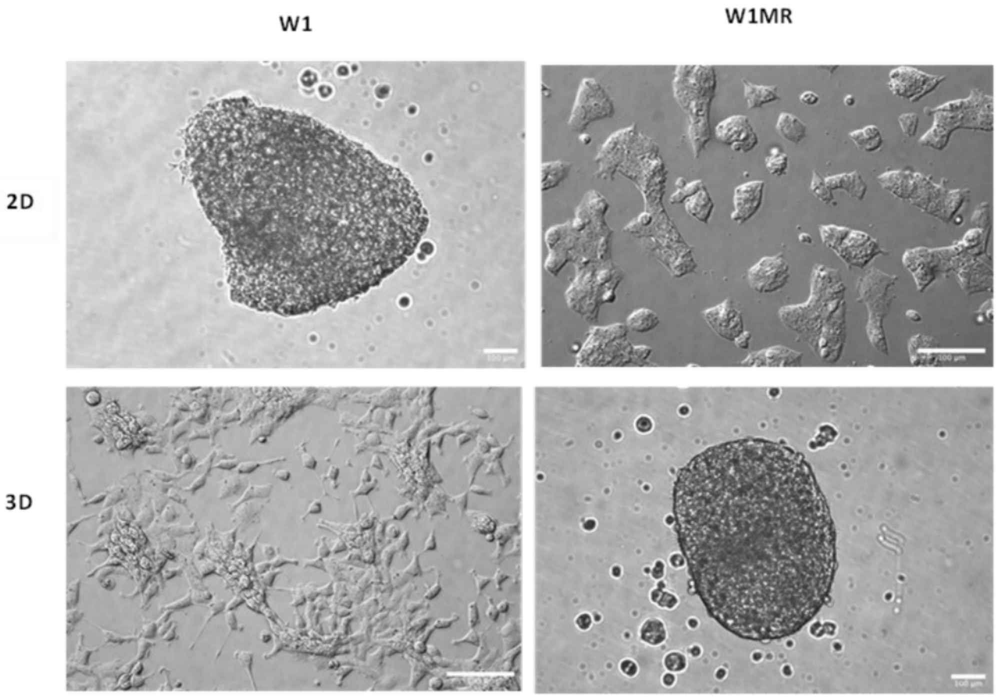

Figure 10. Morphology of drug-sensitive and methotrexate-resistant cell lines growing in 2D and 3D cell culture conditions. Sale bar = 100 μm (20x).

2.9. The Analysis of Methotrexate-Sensitive and Methotrexate–Resistant Cell Lines Viability to Methotrexate Conjugated with Nanoparticles in 2D Culture Condition

For 72 h, both cell lines grew with increased concentrations of APTES-coated and CMC-coated nanoparticles conjugated with methotrexate by ionic or amide bonds. The obtained results compared to free methotrexate are shown in Figure 11, Table 3. For all tested nanoparticles conjugated with methotrexate, we observed decreased cell survival in response to increasing methotrexate concentrations but some differences in responsive curves.

Treating W1 cells with increasing concentrations of APTES-coated or CMC-coated nanoparticles conjugated with methotrexate by ionic bonds decreased the cell viability similar to free methotrexate The IC50 value analysis showed similar resistance 7,74 ng/mL, 17,10 ng/mL adequately compared to 4,29 ng/mL for free methotrexate. Moreover, the response curves in 2D conditions for these forms of drug are almost identical.

The IC50 for W1MR cell lines of free methotrexate and APTES-coated and CMC-coated nanoparticles conjugated with methotrexate by ionic bonds are much higher and the amount is 430,69 ng/mL, 448,69ng/mL, and 409,62 ng/mL respectively. This is in all cases a significant increase of resistance around 100, 58, and 24-fold compared to the sensitive cell line W1. Although the IC50 is similar, the response curves of the W1MR cell line to the achievement of nanoparticles conjugated with methotrexate by ionic bonds compared to free methotrexate are different. Nanoparticles at lower concentrations of MTX appear to be less toxic than free methotrexate.

Concerning the APTES-coated nanoparticles conjugated to methotrexate with stronger amide bonds, we observed a significantly higher IC50 value for the W1 cell line. It was 86,48 ng/mL and the resistance of the W1 cell line is 21,5-fold lower than for free methotrexate. Analyzing the response curve, we observed the characteristic "eye" in the course of both lines suggesting that nanoparticles at lower concentrations appear to be less toxic than free methotrexate. For the W1MR cell line, we observed an 8-fold significant increase in resistance for APTES-coated nanoparticles conjugated to methotrexate with amide bonds in comparison to the sensitive W1 cell line (697,05 ng/mL vs. 86,48 ng/mL, respectively). In this case, also, IC50 for nanoparticles is significantly higher than for free methotrexate (697,05 ng/mL vs. 430,68 ng/mL). This difference is statistically significant.

In summary, the bonding of methotrexate by ionic bonds causes a similar response in sensitive and resistant cell lines. The stronger amide bonding of the drug to the nanoparticles seems to result in both sensitive and resistant lines less sensitive to this form of the drug in this model of culture condition.

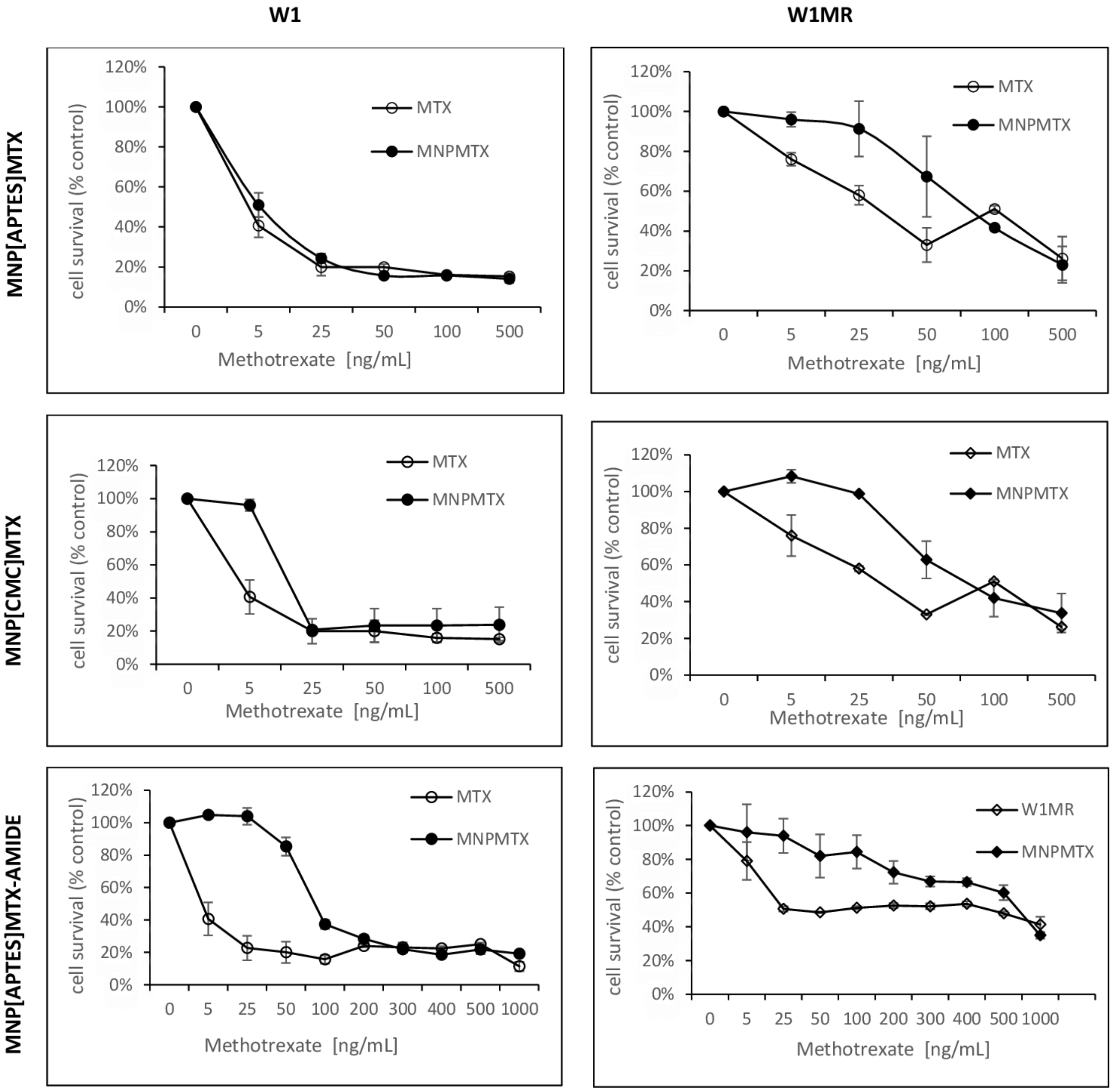

Figure 11. The survival assay of MTT cells in a 2D cell culture condition. Cell line W1 and W1MR were seeded at the density of 10 000cell/well in 96-well plates and treated with increasing concentrations of free MTX and conjugated with nanoparticles MNP[CMC]MTX, MNPs[APTES]MTX or MNPs[APTES]MTXAMID at 37°C for 72h and cell viability was determined. The experiments were repeated at least three times. The level of viability was shown as a percentage of untreated control cells (mean ±SEM).

Table 3. A summary of cell line resistance to cytotoxic drug treatment in 2D cell culture condition.

	W1	W1MR
MTX	4,29 SD ± 0,68 1	430,69 SD± 25,47 100,4 ↑ ***
MNPs[APTES]MTX	7,74 SD± 2,60	448,69 SD± 16,69

	1	58,0 ↑ ***
MNPs[CMC]MTX	17,10 SD± 0,22 1	409,62 SD± 7,36 24,0 ↑ ***
MNPs[APTES]MTXAMID	86,48 SD± 2,33 1	697,05 SD± 55,25 8,1 ↑ ***

2.10. The Analysis of Methotrexate-Sensitive and Methotrexate–Resistant Cell Lines Viability to Methotrexate Conjugated with Nanoparticles in 3D Culture Methods

In the next step, we examined the response to methotrexate conjugated with nanoparticles of the same cells growing as a spheroid. After the formation of spheroids, cells were treated with three different methotrexate-nanocarriers for 72h. The experimental results are presented in Figure 12.

Both tested cell lines were resistant in all methotrexate concentrations even up to 1000 ng/ml MTX reduced cell viability max to 60% in the sensitive and resistant to MTX cell lines. The response to methotrexate conjugated by ionic bonds with nanoparticles was very similar and, in these cases, cell viability remained at 60% almost from the beginning of the tested concentrations of MTX for both the W1 and the W1MR cell lines.

A similar drug concentration-dependent response was also observed in the W1 cell line in response to action APTES-coated nanoparticles conjugated with methotrexate by stronger amide bonds (Figure 12). The cell viability remained at a level of approximately 60 % in the range of methotrexate concentrations tested. The W1MR cell line remained more resistant to this form of drug and was around 90% in the highest tested concentration of MTX. We are unable to determine the IC50 in any of the cell lines either for free methotrexate or for any form of the nanoparticle-bound drug being tested. In 3D culture conditions, it was not possible to overcome the drug resistance of both the sensitive and resistant methotrexate lines in the tested concentrations of methotrexate.

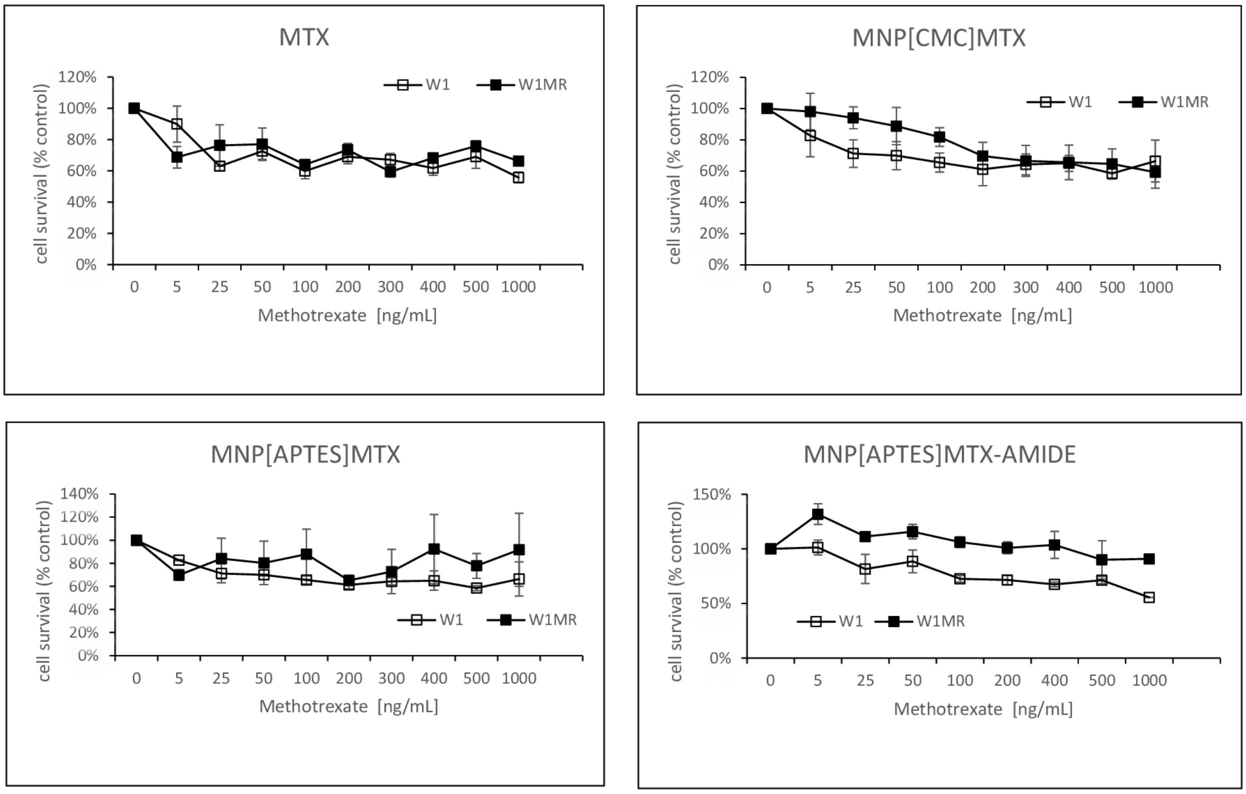

Figure 12. The survival assay of MTT cells in a 3D cell culture condition. Cell line W1 and W1MR were seeded at the density of 25 000cell/well in 96-well plates and treated with increasing concentrations of MTX, MNPs[CMC]MTX, MNPs[APTES]MTX or MNPs[APTES]MTXAMID at 37^{o}C for 72h and cell viability was determined. The experiments were repeated at least three times. The level of viability was shown as a percentage of untreated control cells (mean ±SEM).

3. Discussion

In the above-presented studies, two potential methotrexate nanocarriers based on a magnetic iron oxide Fe_3O_4 core were proposed and tested. Magnetic nanoparticles (MNPs) were functionalized with (3-aminopropyl)triethoxysilane (APTES) or N-carboxymethylchitosan (CMC) as biocompatible polymers and donors of amine or carboxyl groups, respectively. These 10-nanometre structures (TEM) – MNPs[APTES] and MNPs[CMC] - turned out to be non-toxic in vivo tests (MTT assay) towards the tested cell lines, which makes them potentially promising drug carriers in i.e., anticancer therapies. What is worth emphasizing, one of the main mechanisms of MNPs toxicity is considered to be oxidative stress generated by the release of iron ions involved in the Haber-Weiss, Fenton, and Fenton-like reactions which are believed to be the main processes generating reactive oxygen species (ROS) such as superoxide anions, hydroxyl radicals, and hydrogen peroxides [33]. However, there are several reports demonstrating the selectivity of action of MNPs for tumor and normal cells in terms of the level of ROS forming. For example, Ahamed et al. have shown the selectively induced apoptosis in cancer cells (HepG2 and A549) via the p53 pathway by MNPs with no toxicity to normal cells [42]. In another study, it has been reported that exposure to MNPs caused a rise in the production of ROS and reduced the activity of succinate dehydrogenase in complex II of the mitochondria obtained from cancerous oral tongue squamous without significant effects on the control mitochondria [43]. Thus, magnetic iron oxide nanoparticles constitute favourable platforms for drug delivery.

VSM magnetism studies showed a strong magnetic susceptibility of the designed by us nanocarriers, which makes them successful tools in targeted therapy by guiding with an external magnetic field to the tumor site. This results in a significantly reduced toxicity of the chemotherapeutic agent itself for the entire body. Additionally, MNPs[APTES] and MNPs[CMC] demonstrated a significant hyperthermic effect as they generated a temperature increase of up to 45°C in merely a few minutes. This enables the combination of two strategies to destroy the tumor, i.e., targeted delivery of the chemotherapeutic agent and hyperthermia.

MTX attached to APTES – and CMC-coated nanoparticles by ionic bond demonstrated effective release from nanocarriers, which is generally necessary for the drug to act once it reaches the tumor. The release rate of MTX from MNPs[CMC] was moderate, which allows this nanocarrier to be considered suitable for controlled drug release. Additionally, deployment of MNPs[CMC] would avoid the loss of the drug before it reached the target site, and at the same time would result in the effective accumulation of the released, unbound drug in the tumor area. On the other hand, the release of MTX from MNPs[APTES] was rapid, which would probably lead to the loss of a significant amount of the chemotherapeutic agent, e.g., in the blood serum, while delivered to the tumor by guiding with an external magnetic field. However, many favorable features of this carrier, such as ease of synthesis and functionalization, high efficiency of MTX attachment, and lack of toxicity in vitro tests, make it worth considering the modification of the MNPs[APTES]MTX formulation to avoid loss of the drug during delivery. An interesting solution seems to be, for example, the encapsulation of MNPs[APTES]MTX in liposomes. Certainly, the use of MNPs[APTES] as a carrier appears to be appropriate if it is desired to obtain high drug concentrations in a short time. In the case of MTX conjugated with MNPs[APTES] by a solid amide bond, enzymatic activity is required to release the drug. Under the in vitro test conditions (MTT assay), due to the lack of enzymes in the medium, only at higher concentrations of MNPs[APTES]MTX and their accumulation, they were transported inside the tested cells, where the amide bond was enzymatically hydrolyzed. In turn, it resulted in the inhibition of the viability of the cell lines.

Drug resistance in ovarian cancer is still a complex phenomenon that leads to the failure of therapies. We evaluated the response to anticancer methotrexate conjugated with magnetic nanoparticles in different formulations in drug-sensitive and methotrexate-resistant ovarian cancer cell lines. The 2D cell culture model is well-known to scientists. In this model, cells adhere to the surface and are exposed equally to anticancer drugs. Nevertheless, it is not representative of the complexity of tumor tissue, where dense cellular structure and interaction between cells and ECM components may influence drug resistance [44]. We observed a typical concentration-dependent response for form methotrexate conjugated with nanoparticles by ionic bonds used in 2D cell culture conditions that resulted in decreased cell viability with increased drug concentrations. A different curve was obtained for the tested form of the methotrexate bound to nanoparticles with a stronger amide bond. The drug-sensitive W1 cell line was not sensitive to this form of methotrexate in lower concentrations. The methotrexate-resistant cell line was not sensitive to low both free methotrexate and methotrexate conjugated with magnetic nanoparticles concentrations. The higher concentrations of all tested formulations of methotrexate resulted in a concentration-dependent responsive way. Different levels of drug resistance were observed in different formulations of methotrexate. The methotrexate bounding to nanoparticles by ionic bond either by APTES or by CMC caused similar toxicity as free methotrexate. Binding the drug to nanoparticles with a stronger amide bond resulted in a weaker response to the drug by methotrexate-resistant cells under the 2D conditions.

In 2D conditions, resistance to cytotoxic drugs is related to cell-specific mechanisms (mainly expression of membrane transporters). In contrast, in 3D conditions, both cell- and tissue-specific resistance mechanisms (cell density and packing, drug availability) are involved in this process—the change in culture conditions from 2D to 3D causes dramatic changes in drug resistance. Our results indicate that the drug-sensitive and drug-resistant cells cultured in 3D conditions exhibit greater resistance than the cells cultured in 2D conditions against all tested by us formulations of methotrexate: free and conjugated with nanoparticles. According to recent data, 3D models of cell cultures have characteristic features that affect the development of drug resistance. None of the forms of methotrexate we investigated overcame the drug resistance of ovarian cancer cells in the 3D model we tested. Both the W1 and W1MR cell lines formed very similar dense spheroids. There are similarities in the response to free MTX. The W1 and W1MR spheroids were sensitive beginning from low MTX concentrations, which reduced spheroid viability from 80% in control to a maximum reduction of 60% in control at concentrations of 1000 ng/mL of MTX. Nevertheless, further increases in MTX concentrations in both spheroids did not result in reduced spheroids' viability. It could be due to the insensitivity of quiescent cells in the medium zone of the spheroid to MTX. A further possible reason is the limited properties of MTX to diffuse through dense cellular structure, which is about the size of the spheroids. This theory was proved by West et al. [45] in patients with primary osteosarcoma with different responsiveness to MTX.

The effectiveness of drugs in spheroids depends on various factors such as the size and the structure of the spheroid (dense or loose), the cell type (necrotic, quiescent, proliferating cells), drug concentrations, drug diffusion into the dense cellular/ECM structure and expression of drug resistance genes and proteins encoding by these genes. Given the organization of tumor tissue, drugs associated with magnetic nanoparticles appear to have the potential to penetrate and release into the tumor, resulting in an increased toxicity effect against tumor cells.

Not surprisingly, methotrexate bound to nanoparticles by an ionic bond, which is released rapidly in the environment, acts similarly to free methotrexate. We see greater potential in drugs associated with magnetic iron oxide nanoparticles with a stronger amide bond. The results indicate that MNPs-conjugated drug in lower doses has a low toxic effect on ovarian cancer cells, and their IC50 is 20 times higher than that of free methotrexate in 2D conditions. In 3D conditions, its effect is similar to that of other drug forms on the sensitive line and 20% weaker on the methotrexate-resistant line. However, we are convinced that the weaker effect of the MNPs-conjugated MTX was caused by the necessity to penetrate the cells, where the enzymatic activity ensured the hydrolysis of the amide bond. Nevertheless, we speculate that in the real tumor environment, the high proteinase activity would guarantee an effective drug release and thus provide a high cytotoxicity effect. Moreover, drug nanocarriers guided by an external magnetic field and accumulated within the tumor would limit the overall toxicity to the body that would be caused by an unbound chemotherapeutic. If we additionally consider the phenomenon of hyperthermia, it appears that magnetic nanocarriers constitute a much better alternative than the classically used form of drugs.

Understanding how drug resistance mechanisms occur using spheroids may help to develop more effective anticancer therapies. It is crucial to consider the aim of the study as the best model. These studies have several require further research on a modified 3D model that considers not only spheroids of similar size and density as tumors. It is also important to create a research model that considers the components of the extracellular matrix (ECM) that also contain the necessary proteinases, fibroblasts that are secreting transforming growth factors, effective angiogenic stimulators, and changes in pH inside cancerous tumors.

4. Materials and Methods

4.1. Synthesis of Magnetic Fe_3O_4 Nanoparticles (MNPs)

MNPs were synthesized using the chemical co-precipitative method [46]. However, the method was modified in terms of the reaction temperature as well as in terms of the concentration of the used ammonia solution. In the typical experimental procedure, 8.11 g of iron (III) chloride hexahydrate ($FeCl_3 \cdot 6H_2O$) and 5.96 of iron (II) chloride tetrahydrate ($FeCl_2 \cdot 4H_2O$) were diluted in 100 ml of distilled water, respectively, and added into a three-necked flask. The mixture was vigorously stirred using a mechanical stirrer, heated to 70°C, and purged with N_2. Next, the ammonia solution ($NH_3 \cdot H_2O$) was slowly added (1 drop per 1-2 seconds) to bring to pH = 9.0. The black MNPs precipitate was washed three times with distilled water and then with methanol. Followingly, MNPs were suspended in 200 ml of 50 mM TMAOH and sonicated for 1 hour in an ultrasonic cleaner. The black MNPs precipitate was pulled away by a magnet, washed with distilled water and methanol, and dried in a drying chamber at 50°C for 12 h.

4.2. Surface Modification of Nanoparticles with (3- Aminopropyl)trimethoxysilane (APTES) and N-Carboxymethyl Chitosan (CMC)

MNPs functionalization with APTES was carried out using the method used by Cao et al. [47]. Briefly, 600 mg of MNPs was dispersed into a mixture of 100 ml distilled water and 150 ml of isopropanol by ultrasonic vibration for 1 h. Then, 30 ml of concentrated (25%) NH_3 and 1.3 ml of APTES were added to the mixture under constant mechanical stirring and heating (55°C) for 20 hours. After the reaction, the brown precipitate was washed three times with water and next with methanol and dried at 35°C for 24 h in a drying chamber.

MNPs functionalization with CMC was carried out using the method designed by us. 600 mg MNPs were suspended in the mixture of 75 ml isopropanol and 50 ml distilled water and sonicated in an ultrasonic cleaner for 1 h. 30 ml of distilled water was added to 300 mg CMC and the mixture was stirred until the complete dissolution. Then, CMC solution was added to the suspension of MNPs and sonicated for the next 30 minutes. Next, the mixture was stirred using a mechanical stirrer at 55°C for 20 hours. After the reaction, the brown precipitate was washed three times with water and next with methanol and dried at 35°C for 24 h in a drying chamber.

4.3. Characterization with FT-IR and Transmission Electron Microscope (TEM) Imaging of APTES- and CMC-Modified Nanoparticles (MNPs[APTES] and CMC[APTES])

2 mg of MNPs[APTES] or MNPs[CMC], respectively, were added to 200 mg of KBr and rubbed in the mortar. Then, a small sample of the mixture was pressed using a hydraulic press (Sirio) into a pellet. Fourier transform infrared (FT-IR) spectra were acquired using an IR Spirit (Shimadzu) spectrometer in the range of 4000-400 cm^{-1}. TEM images were performed using a transmission microscope Titan G2 60-300 (FEI).

4.4. Magnetic VSM Properties Measurements of MNPs[APTES] and MNPs[CMC]

Magnetometry measurements were made using a vibration magnetometer type 7407 from LakeShore, equipped with a liquid nitrogen-cooled flow cryostat. Measurements of the temperature dependence of magnetization curves were made for each sample magnetization for selected temperatures. The first type of measurement (MvT) allows the examination of the magnetic nature of the samples, in particular, the estimation of the blocking temperature (T_b) based on the inflection point and maximum of the $M_{ZFC}(T)$ curve (*ZFC – Zero Field-Cooled*) [48]. The blocking temperature is defined as the transition temperature from the blocked state magnetic moments to the superparamagnetic state. At blocking temperature, the hysteresis loop disappears because the thermal fluctuations of the magnetic moments are enough large that the average magnetization without an external magnetic field is zero. The transition from the locked state to the superparamagnetic state usually occurs at one critical point temperature characteristic of a given system. MvT measurements were performed using the following sequence: (i) heating the sample to T=440 K in H=0, (ii) cooling the sample to T=90 K in H=0, (iii) measurement of the ZFC relationship while heating the sample in a constant field H=100 Oe, (iv) measurement of the relationship FC (*FC - Field-Cooled*) when cooling the sample in a constant field H=100 Oe.

The second type of measurement (MvHvT) allows for the estimation of temperature dependencies of saturation magnetization (based on the *approach to saturation model* [49]) and remanence and coercive field, i.e., parameters indicating the expected superparamagnetic nature of the tested materials. Full hysteresis loops were tested in magnetic field strength range up to 16.5 kOe. The loops were collected at temperatures T = 100, 120, 140, 170, 200, 250, 300, 360, 440K.

4.5. Hyperthermic Properties of MNPs[APTES] and MNPs[CMC]

Hyperthermal properties of nanoparticle solutions (4 mg/ml) were studied using induction equipment heating by DACPOL. The control system was equipped with a transistor generator (by AMBRELL) of high frequency to induction heating (EASY Heat 0224FFCE) with a power of up to 2.4 kW, component power supply system, and system controlling the current, power, and sample heating time. The cooling system (TEXA TCW12NBSBCP0000) was connected to the generator and the induction coil. The generator converts the supply voltage of 240 V with a frequency of 50 Hz into the voltage of frequencies in the 150-450 kHz range. The record of temperature increase as a function of time (under the influence of an external electromagnetic field, at given current strengths) was carried out from a temperature of 36.6°C to 45°C.

4.6. Attaching Methotrexate (MTX) to the APTES-Coated and CMC-Coated MNPs by Ionic Bonds

600 mg of MNPs[APTES] or MNPs[CMC], respectively, were suspended in 60 ml of phosphate buffer (pH=6.0) and sonicated in an ultrasonic cleaner for 30 minutes with simultaneous cooling. 30 mg of MTX was dissolved in the mixture of phosphate buffer (pH=6.0) and DMSO (1:1, 30 ml). Next, the solution of MTX was slowly instilled into the suspension of nanoparticles during continuous sonication. The suspension containing MTX was sonicated for the next 15 minutes. After that, the mixture was stirred using a mechanical stirrer for 20 h at room temperature. The nanoparticles were pulled away by a magnet, washed with distilled water (2 x 60 ml), and methanol (2 x 60 ml), and dried at 30°C for 24 hours in a drying chamber.

A method of the MTX loading capacity quantitation made use of the fact that $KHSO_4$ causes the complete removal of the drug from its salts with APTES or CMC. The basics of the method were formerly reported [50]. Briefly, a sample of MNP[APTES]MTX or MNPs[CMC]MTX (5 mg) was suspended in 2 mL of the mixture of 0.1 M $KHSO_4$ (pH=1.5) and DMSO (4:1) and sonicated for 15 min in an ultrasonic cleaner. After separating the nanoparticles (MNP[APTES] or MNPs[CMC], respectively) with a magnet, the solution was centrifugated (13000 rpm, 10 min, 25°C) and the concentration of the released drug in the supernatant was measured using a UV-VIS spectrophotometer (2450 UV-VIS Shimadzu) at wavelength λ=370 nm. The measurements were repeated in three independent trials with satisfactory reproducibility of results.

4.7. Attaching Methotrexate (MTX) to the APTES-Coated MNPs by Amide Bond

To conjugate the MTX on the surface of MNPs[APTES] by amide bond, 1g of MNPs[APTES] were dispersed in the mixture of 50 ml of DMSO and 10 ml of distilled water and sonicated for 20 minutes in an ultrasonic cleaner. Then, 50 mg of free MTX, 105 mg of EDC hydrochloride, and 63.2 mg of N-hydroxysuccinimide (NHS) were dissolved in 20 ml of DMSO, and the mixture was added to the suspension of nanoparticles. The pH of the solution was adjusted to 8.2 by the triethylamine addition. The resulting suspension was stirred overnight (20 h) at room temperature (~22 °C) in the dark. Following MTX conjugation, the modified nanoparticles were isolated with an external magnet, washed with distilled water (2 x 60 ml), and methanol (2 x 60 ml), and dried at 30°C for 24 hours in a drying chamber.

The MTX loading capacity quantification was performed using proteinase K. Proteinase K was dissolved in 2 ml of PBS buffer (pH=7.5) to obtain a final enzyme concentration equal to 1 mg/ml. The mixture was added to the nanoparticles (5 mg) and incubated at 37°C for 3 h. After that time, the solution was centrifugated (13000 rpm, 10 min, 25°C), and the concentration of the released drug in the supernatant was measured using a UV-VIS spectrophotometer (2450 UV-VIS Shimadzu) at wavelength λ=370 nm. The measurements were repeated in three independent trials with satisfactory reproducibility of results.

4.8. DLS and Zeta Potential Measurements of MNPs, MNPs[APTES], MNPs[CMC] and MTX-Functionalized Nanoparticles (MNPs[APTES]MTX and MNPs[CMC]MTX)

The hydrodynamic size distribution was measured by the dynamic light scattering (DLS) method using a Zetasizer Nano-ZS instrument (Malvern, Poland). Samples were suspended in buffer (pH=7.5, 0.1 mg/mL) and measured 3 times with 15 runs at 25°C. The zeta-potential was measured by laser Doppler velocimetry using the same instrument. Samples were suspended in buffer (pH=7.5, 0.1 mg/mL) and measured 3 times with 30 runs. The composition of the buffer corresponded to the composition of the RPMI 1640 medium ($Ca(NO_3)_2 \times 4H_2O$ 0.1 g/L, KCl 0.4 g/L, $MgSO_4 \times 7H_2O$ 0.1 g/L, NaCl 6 g/L, $NaHCO_3$ 2 g/L, Na_2HPO_4 0.8 g/L, D-glucose 2 g/L) (www.capricorn-scientific.com).

4.9. Investigation of MTX Release from MNPs[APTES]MTX and MNPs[CMC]MTX (Ionic bond)

5 mg of MNPs[APTES]MTX (ionic bond) or 20 mg of MNPs[CMC]MTX, respectively, were dispersed in 2 mL of buffer (pH= 7.5 or 6.0) and incubated at 37°C or 45°C for 24 h. At specified time intervals, nanoparticles were pulled away with a magnet, and the solution after separation was centrifugated (13000 rpm, 5 min, 25°C). The concentration of a released drug in the supernatant was determined on a UV-VIS spectrophotometer (2450 UV-VIS Shimadzu) at wavelength λ=370 nm. To the remaining nanoparticles after sample separation, 2 mL of fresh buffer was added, and the incubation at 37°C of the sample was continued until the next measurement. Continuous removal of the released drug was necessary; otherwise, the equilibrium state of dissociation of the salt ($APTES^+MTX^-$ or CMC^-MTX^+) was reached. The experiments were performed three times with satisfactory reproducibility of results. The composition of the buffer corresponded to the composition of the RPMI 1640 medium ($Ca(NO_3)_2 \times 4H_2O$ 0.1 g/L, KCl 0.4 g/L, $MgSO_4 \times 7H_2O$ 0.1 g/L, NaCl 6 g/L, $NaHCO_3$ 2 g/L, Na_2HPO_4 0.8 g/L, D-glucose 2 g/L) (www.capricorn-scientific.com). The specific pH was adjusted using a pH-meter by the addition of sodium acid phosphate ($NaH_2PO_4 \times 2H_2O$, 0.8 g/L).

4.10. Investigation of MTX Release from MNPs[APTES]MTX (Amide Bond)

10 mg of MTX-grafted nanoparticles were suspended in a solution of 0.1 mg/mL protease K in 2 ml of phosphate-buffered saline (PBS, pH=7.5) and incubated at 37 °C under constant stirring. The solution pH of 2.0 and 6.0, respectively, was adjusted by the titration of 1.0 M HCl. Following incubation for 1, 6, and 24 h, the nanoparticle suspensions were centrifuged (13000 rpm, 5 min, 25°C) and the concentration of a released drug in the supernatant was determined on a UV-VIS spectrophotometer (2450 UV-VIS Shimadzu) at wavelength λ=370 nm.

4.11. Cell Lines and Cell Culture

In this study, we used the W1 ovarian cancer cell line, established from ovarian cancer tissue from an untreated patient, and the methotrexate-resistant cell line W1MR as described previously [51]. IC50 between W1 and W1MR cell lines showed a high increase in resistance to MTX. The final concentration MTX used to select the resistant cells was - 28 ng/ml. Both cell lines were harvested in RPMI-1640 medium supplemented with 2 pML-glutamine, FBS (10% v/v), penicillin (100 units/ml), streptomycin (100 units/ml), and amphotericin B (25 g/ml). Cells were grown at 37 ◦C in a 5% CO2 atmosphere in T25 and T75 flasks (Googlab Scientific). Cytotoxic drugs, RPMI-1640 medium, and FBS were acquired from Sigma (St. Louis, MO, USA). The antibiotic-antimycotic solution was obtained from Corning (New York, USA).

4.12. 2D (Two-Dimensional) and 3D (Three-Dimensional) Cell Culture Morphology

For the growth of cells in adherent 2D cell cultures, cells were trypsinized using 0.25% Trypsin (Corning), resuspended in 1 ml of the growth medium, and transferred to 6-well plates in an amount of 250,000 cells per well. The cell culture was conducted for five days, and the medium was changed every two days. An inverted microscope was used to evaluate the morphology of drug-sensitive and resistant cell lines.

In 3D cell cultures, cells formed spheroids. The cells were trypsinized, resuspended in 200 µL of the growth medium, and transferred to nonadherent surface 96-wells plates (BRAND plates inter Grade, F-bottom, 781902 (Merck) in an amount of 10 000 cells per well. The cell culture was conducted for five days, and the medium was changed every two days. Spheroid morphology of drug-sensitive and resistant cell lines was evaluated using an inverted microscope (Primovert Zeiss).

4.13. MTT Assay

The drug sensitivity/resistance was measured using the MTT assay. Initially, cells were seeded in the 96-well plates: 10,000 cells per well (2D) and 25,000 for 3D cell culture per well. After 48 h of culture, the medium was replaced with fresh medium with or without free methotrexate (as positive control) and APTES-coated or CMC-coated nanoparticles conjugated with methotrexate by ionic or amid bonds in increasing concentrations, and the cells were incubated at 37 ◦C in a 5% CO2 atmosphere for 72 h. Afterward, 10 µL of the MTT (4mg/mL) was added, and cells were incubated for 4 h under the same conditions. After this time, 100 µL of 10% SDS in 0.01M HCl was added. The cell culture was continued until the following day. The absorbance was measured at 570 nm using a microplate reader with a reference wavelength of 720 nm (Synergy 2 Multi-Detectin Microplate Reader by BioTek Instruments, Inc.) and analyzed by Gen5 software. As a negative control, we used a sample containing all components cell culture medium, MTT, and SDS solution without cells. The experiments were repeated three times, and each sample with an appropriate nanoparticle concentration was doubled. For all forms of magnetic nanoparticles conjugated with methotrexate in investigated cell lines, the IC50 value was determined.

5. Conclusions

Iron oxide (Fe_3O_4) nanoparticles functionalized with (3-aminopropyl)triethoxysilane (APTES) or N-carboxymethylchitosane (CMC) were synthesized to obtain nanostructures with significant magnetic and hyperthermic properties. The coating polymers provide amino and carboxyl groups, respectively, which can be used to attach bioactive compounds using ionic or strong covalent bonds, such as amide bonds. Importantly, MNPs[APTES] and MNPs[CMC] turned out to be non-toxic (*in vitro* tests), which makes them potential drug nanocarriers. Methotrexate attached to MNPs[CMC] was released moderately at pH = 6.0 and 7.5 and temperatures of 37°C and 45°C, which indicates controlled release of the drug. MTX attached to MNPs[APTES] via an amide bond was released effectively at low pH, i.e., in conditions corresponding to the environment inside cell lysosomes. The tested drug conjugated with MNPs[APTES] via an ionic bond was released rapidly, which may be an advantage within the tumour, provided that the nanocarrier is delivered in a form that prevents the loss of the drug in the bloodstream. The solution may be encapsulating MNPs[APTES]MTX (ionic bond) in liposomes. MTX-immobilized nanoparticles were incubated with ovarian cancer cell lines in 2D and 3D conditions. The results of cytotoxicity tests showed similar values of cell proliferation inhibition for both the free drug and the drug bound to nanoparticles. The conjugation of MTX with nanoparticles gives it an additional feature that means that the drug can be directed to the target site using an external magnetic field, which translates into less toxicity to the body. Moreover, considering the possibility of combining chemotherapy with a hyperthermic effect, it can be assumed that the drug immobilized on MNPs would exhibit a greater therapeutic effect in vivo than free MTX. However, this requires additional research on advanced 3D models.

Acknowledgments: We would like to express special thanks to prof. Radosław Januchowski for providing cell lines and consultations on 3D analysis.

Contribution: Julia Nowak-Jary: synthesis and functionalization of magnetic nanoparticles, characteristics of physicochemical properties of magnetic nanoparticles, drug release studies, manuscript preparing; Artur Płóciennik: cytotoxicity studies; Beata Machnicka: cytotoxicity studies, supervised the study and reviewed the manuscript. All authors read and approved the final manuscript.

Competing interests: The authors declared no potential conflicts of interest with respect to the research, authorship, and publication of this article.

References

1. Bao, Y.; Sherwood, J.A.; Sun, Z. Magnetic Iron Oxide Nanoparticles as T_1 Contrast Agents for Magnetic Resonance Imaging. *J. Mater. Chem. C* **2018**, *6*, 1280–1290, doi:10.1039/C7TC05854C.
2. Huang, J.; Zhong, X.; Wang, L.; Yang, L.; Mao, H. Improving the Magnetic Resonance Imaging Contrast and Detection Methods with Engineered Magnetic Nanoparticles. *Theranostics* **2012**, *2*, 86–102, doi:10.7150/thno.4006.
3. Zhou, Q.; Wei, Y. For Better or Worse, Iron Overload by Superparamagnetic Iron Oxide Nanoparticles as a MRI Contrast Agent for Chronic Liver Diseases. *Chem. Res. Toxicol.* **2017**, *30*, 73–80, doi:10.1021/acs.chemrestox.6b00298.
4. Russell, E.; Dunne, V.; Russell, B.; Mohamud, H.; Ghita, M.; McMahon, S.J.; Butterworth, K.T.; Schettino, G.; McGarry, C.K.; Prise, K.M. Impact of Superparamagnetic Iron Oxide Nanoparticles on in Vitro and in Vivo Radiosensitisation of Cancer Cells. *Radiat Oncol* **2021**, *16*, 104, doi:10.1186/s13014-021-01829-y.
5. Palzer, J.; Eckstein, L.; Slabu, I.; Reisen, O.; Neumann, U.P.; Roeth, A.A. Iron Oxide Nanoparticle-Based Hyperthermia as a Treatment Option in Various Gastrointestinal Malignancies. *Nanomaterials* **2021**, *11*, 3013, doi:10.3390/nano11113013.
6. Obaidat, I.M.; Narayanaswamy, V.; Alaabed, S.; Sambasivam, S.; Muralee Gopi, C.V.V. Principles of Magnetic Hyperthermia: A Focus on Using Multifunctional Hybrid Magnetic Nanoparticles. *Magnetochemistry* **2019**, *5*, 67, doi:10.3390/magnetochemistry5040067.
7. Mu, X.; Li, J.; Yan, S.; Zhang, H.; Zhang, W.; Zhang, F.; Jiang, J. siRNA Delivery with Stem Cell Membrane-Coated Magnetic Nanoparticles for Imaging-Guided Photothermal Therapy and Gene Therapy. *ACS Biomater. Sci. Eng.* **2018**, *4*, 3895–3905, doi:10.1021/acsbiomaterials.8b00858.
8. Usković, V.; Tang, S.; Wu, V.M. Targeted Magnetic Separation of Biomolecules and Cells Using Earthicle-Based Ferrofluids. *Nanoscale* **2019**, *11*, 11236–11253, doi:10.1039/C9NR01579E.
9. El-Boubbou, K. Magnetic Iron Oxide Nanoparticles as Drug Carriers: Clinical Relevance. *Nanomedicine* **2018**, *13*, 953–971, doi:10.2217/nnm-2017-0336.
10. Bukowski, K.; Kciuk, M.; Kontek, R. Mechanisms of Multidrug Resistance in Cancer Chemotherapy. *IJMS* **2020**, *21*, 3233, doi:10.3390/ijms21093233.
11. Duan, C.; Yu, M.; Xu, J.; Li, B.-Y.; Zhao, Y.; Kankala, R.K. Overcoming Cancer Multi-Drug Resistance (MDR): Reasons, Mechanisms, Nanotherapeutic Solutions, and Challenges. *Biomedicine & Pharmacotherapy* **2023**, *162*, 114643, doi:10.1016/j.biopha.2023.114643.
12. Fan, J.; To, K.K.W.; Chen, Z.-S.; Fu, L. ABC Transporters Affects Tumor Immune Microenvironment to Regulate Cancer Immunotherapy and Multidrug Resistance. *Drug Resistance Updates* **2023**, *66*, 100905, doi:10.1016/j.drup.2022.100905.
13. Patel, N.R.; Pattni, B.S.; Abouzeid, A.H.; Torchilin, V.P. Nanopreparations to Overcome Multidrug Resistance in Cancer. *Advanced Drug Delivery Reviews* **2013**, *65*, 1748–1762, doi:10.1016/j.addr.2013.08.004.
14. Fletcher, J.I.; Williams, R.T.; Henderson, M.J.; Norris, M.D.; Haber, M. ABC Transporters as Mediators of Drug Resistance and Contributors to Cancer Cell Biology. *Drug Resistance Updates* **2016**, *26*, 1–9, doi:10.1016/j.drup.2016.03.001.

15. Mansoori, B.; Mohammadi, A.; Davudian, S.; Shirjang, S.; Baradaran, B. The Different Mechanisms of Cancer Drug Resistance: A Brief Review. *Adv Pharm Bull* **2017**, *7*, 339–348, doi:10.15171/apb.2017.041.
16. Correia, A.L.; Bissell, M.J. The Tumor Microenvironment Is a Dominant Force in Multidrug Resistance. *Drug Resistance Updates* **2012**, *15*, 39–49, doi:10.1016/j.drup.2012.01.006.
17. Rahmanian, M.; Seyfoori, A.; Ghasemi, M.; Shamsi, M.; Kolahchi, A.R.; Modarres, H.P.; Sanati-Nezhad, A.; Majidzadeh-A, K. In-Vitro Tumor Microenvironment Models Containing Physical and Biological Barriers for Modelling Multidrug Resistance Mechanisms and Multidrug Delivery Strategies. *Journal of Controlled Release* **2021**, *334*, 164–177, doi:10.1016/j.jconrel.2021.04.024.
18. Tan, Q.; Saggar, J.K.; Yu, M.; Wang, M.; Tannock, I.F. Mechanisms of Drug Resistance Related to the Microenvironment of Solid Tumors and Possible Strategies to Inhibit Them. *The Cancer Journal* **2015**, *21*, 254–262, doi:10.1097/PPO.0000000000000131.
19. Muz, B.; De La Puente, P.; Azab, F.; Azab, A.K. The Role of Hypoxia in Cancer Progression, Angiogenesis, Metastasis, and Resistance to Therapy. *HP* **2015**, 83, doi:10.2147/HP.S93413.
20. Padera, T.P.; Meijer, E.F.J.; Munn, L.L. The Lymphatic System in Disease Processes and Cancer Progression. *Annu. Rev. Biomed. Eng.* **2016**, *18*, 125–158, doi:10.1146/annurev-bioeng-112315-031200.
21. Turley, S.J.; Cremasco, V.; Astarita, J.L. Immunological Hallmarks of Stromal Cells in the Tumour Microenvironment. *Nat Rev Immunol* **2015**, *15*, 669–682, doi:10.1038/nri3902.
22. Westhoff, M.A.; Zhou, S.; Bachem, M.G.; Debatin, K.M.; Fulda, S. Identification of a Novel Switch in the Dominant Forms of Cell Adhesion-Mediated Drug Resistance in Glioblastoma Cells. *Oncogene* **2008**, *27*, 5169–5181, doi:10.1038/onc.2008.148.
23. Garcia-Mayea, Y.; Mir, C.; Masson, F.; Paciucci, R.; LLeonart, M.E. Insights into New Mechanisms and Models of Cancer Stem Cell Multidrug Resistance. *Seminars in Cancer Biology* **2020**, *60*, 166–180, doi:10.1016/j.semcancer.2019.07.022.
24. Nowacka, M.; Sterzynska, K.; Andrzejewska, M.; Nowicki, M.; Januchowski, R. Drug Resistance Evaluation in Novel 3D in Vitro Model. *Biomedicine & Pharmacotherapy* **2021**, *138*, 111536, doi:10.1016/j.biopha.2021.111536.
25. Kapałczyńska, M.; Kolenda, T.; Przybyła, W.; Zajączkowska, M.; Teresiak, A.; Filas, V.; Ibbs, M.; Bliźniak, R.; Łuczewski, Ł.; Lamperska, K. 2D and 3D Cell Cultures – a Comparison of Different Types of Cancer Cell Cultures. *aoms* **2016**, doi:10.5114/aoms.2016.63743.
26. Weaver, V.M.; Lelièvre, S.; Lakins, J.N.; Chrenek, M.A.; Jones, J.C.R.; Giancotti, F.; Werb, Z.; Bissell, M.J. B4 Integrin-Dependent Formation of Polarized Three-Dimensional Architecture Confers Resistance to Apoptosis in Normal and Malignant Mammary Epithelium. *Cancer Cell* **2002**, *2*, 205–216, doi:10.1016/S1535-6108(02)00125-3.
27. Pampaloni, F.; Reynaud, E.G.; Stelzer, E.H.K. The Third Dimension Bridges the Gap between Cell Culture and Live Tissue. *Nat Rev Mol Cell Biol* **2007**, *8*, 839–845, doi:10.1038/nrm2236.
28. Li, C.; Kato, M.; Shiue, L.; Shively, J.E.; Ares, M.; Lin, R.-J. Cell Type and Culture Condition–Dependent Alternative Splicing in Human Breast Cancer Cells Revealed by Splicing-Sensitive Microarrays. *Cancer Research* **2006**, *66*, 1990–1999, doi:10.1158/0008-5472.CAN-05-2593.
29. Świerczewska, M.; Sterzyńska, K.; Ruciński, M.; Andrzejewska, M.; Nowicki, M.; Januchowski, R. The Response and Resistance to Drugs in Ovarian Cancer Cell Lines in 2D Monolayers and 3D Spheroids. *Biomedicine & Pharmacotherapy* **2023**, *165*, 115152, doi:10.1016/j.biopha.2023.115152.
30. Lee, J.; Cuddihy, M.J.; Kotov, N.A. Three-Dimensional Cell Culture Matrices: State of the Art. *Tissue Engineering Part B: Reviews* **2008**, *14*, 61–86, doi:10.1089/teb.2007.0150.
31. Vinci, M.; Gowan, S.; Boxall, F.; Patterson, L.; Zimmermann, M.; Court, W.; Lomas, C.; Mendiola, M.; Hardisson, D.; Eccles, S.A. Advances in Establishment and Analysis of Three-Dimensional Tumor Spheroid-Based Functional Assays for Target Validation and Drug Evaluation. *BMC Biol* **2012**, *10*, 29, doi:10.1186/1741-7007-10-29.
32. Marushima, H. Three-Dimensional Culture Promotes Reconstitution of the Tumor-Specific Hypoxic Microenvironment under TGFβ Stimulation. *Int J Oncol* **2011**, doi:10.3892/ijo.2011.1142.
33. Wu, H.; Yin, J.-J.; Wamer, W.G.; Zeng, M.; Lo, Y.M. Reactive Oxygen Species-Related Activities of Nano-Iron Metal and Nano-Iron Oxides. *Journal of Food and Drug Analysis* **2014**, *22*, 86–94, doi:10.1016/j.jfda.2014.01.007.
34. Sabouri, Z.; Sabouri, M.; Moghaddas, S.S.T.H.; Darroudi, M. Design and Preparation of Amino-Functionalized Core-Shell Magnetic Nanoparticles for Photocatalytic Application and Investigation of Cytotoxicity Effects. *J Environ Health Sci Engineer* **2022**, *21*, 93–105, doi:10.1007/s40201-022-00842-x.
35. Ghutepatil, P.R.; Salunkhe, A.B.; Khot, V.M.; Pawar, S.H. APTES (3-Aminopropyltriethoxy Silane) Functionalized MnFe2O4 Nanoparticles: A Potential Material for Magnetic Fluid Hyperthermia. *Chem. Pap.* **2019**, *73*, 2189–2197, doi:10.1007/s11696-019-00768-z.
36. Comanescu, C. Recent Advances in Surface Functionalization of Magnetic Nanoparticles. *Coatings* **2023**, *13*, 1772, doi:10.3390/coatings13101772.

37. Wildeboer, R.R.; Southern, P.; Pankhurst, Q.A. On the Reliable Measurement of Specific Absorption Rates and Intrinsic Loss Parameters in Magnetic Hyperthermia Materials. *J. Phys. D: Appl. Phys.* **2014**, *47*, 495003, doi:10.1088/0022-3727/47/49/495003.
38. Lachowicz, D.; Górka, W.; Kmita, A.; Bernasik, A.; Żukrowski, J.; Szczerba, W.; Sikora, M.; Kapusta, C.; Zapotoczny, S. Enhanced Hyperthermic Properties of Biocompatible Zinc Ferrite Nanoparticles with a Charged Polysaccharide Coating. *J. Mater. Chem. B* **2019**, *7*, 2962–2973, doi:10.1039/C9TB00029A.
39. Kmita, A.; Lachowicz, D.; Żukrowski, J.; Gajewska, M.; Szczerba, W.; Kuciakowski, J.; Zapotoczny, S.; Sikora, M. One-Step Synthesis of Long Term Stable Superparamagnetic Colloid of Zinc Ferrite Nanorods in Water. *Materials* **2019**, *12*, 1048, doi:10.3390/ma12071048.
40. Maguire, C.M.; Rösslein, M.; Wick, P.; Prina-Mello, A. Characterisation of Particles in Solution - a Perspective on Light Scattering and Comparative Technologies. *Sci Technol Adv Mater* **2018**, *19*, 732–745, doi:10.1080/14686996.2018.1517587.
41. De Milito, A.; Fais, S. Tumor Acidity, Chemoresistance and Proton Pump Inhibitors. *Future Oncol.* **2005**, *1*, 779–786, doi:10.2217/14796694.1.6.779.
42. Ahamed, M.; Alhadlaq, H.A.; Khan, M.A.M.; Akhtar, Mohd.J. Selective Killing of Cancer Cells by Iron Oxide Nanoparticles Mediated through Reactive Oxygen Species via P53 Pathway. *J Nanopart Res* **2013**, *15*, 1225, doi:10.1007/s11051-012-1225-6.
43. Jahanbani, J.; Ghotbi, M.; Shahsavari, F.; Seydi, E.; Rahimi, S.; Pourahmad, J. Selective Anticancer Activity of Superparamagnetic Iron Oxide Nanoparticles (SPIONs) against Oral Tongue Cancer Using in Vitro Methods: The Key Role of Oxidative Stress on Cancerous Mitochondria. *J Biochem Mol Toxicol* **2020**, *34*, doi:10.1002/jbt.22557.
44. Xu, X.; Farach-Carson, M.C.; Jia, X. Three-Dimensional in Vitro Tumor Models for Cancer Research and Drug Evaluation. *Biotechnology Advances* **2014**, *32*, 1256–1268, doi:10.1016/j.biotechadv.2014.07.009.
45. West, G.W.; Weichselbaum, R.; Little, J.B. Limited Penetration of Methotrexate into Human Osteosarcoma Spheroids as a Proposed Model for Solid Tumor Resistance to Adjuvant Chemotherapy. *Cancer Res* **1980**, *40*, 3665–3668.
46. Massart, R. Preparation of Aqueous Magnetic Liquids in Alkaline and Acidic Media. *IEEE Trans. Magn.* **1981**, *17*, 1247–1248, doi:10.1109/TMAG.1981.1061188.
47. Cao, H.; He, J.; Deng, L.; Gao, X. Fabrication of Cyclodextrin-Functionalized Superparamagnetic Fe3O4/Amino-Silane Core–Shell Nanoparticles via Layer-by-Layer Method. *Applied Surface Science* **2009**, *255*, 7974–7980, doi:10.1016/j.apsusc.2009.04.199.
48. Bruvera, I.J.; Mendoza Zélis, P.; Pilar Calatayud, M.; Goya, G.F.; Sánchez, F.H. Determination of the Blocking Temperature of Magnetic Nanoparticles: The Good, the Bad, and the Ugly. *Journal of Applied Physics* **2015**, *118*, 184304, doi:10.1063/1.4935484.
49. Zhang, H.; Zeng, D.; Liu, Z. The Law of Approach to Saturation in Ferromagnets Originating from the Magnetocrystalline Anisotropy. *Journal of Magnetism and Magnetic Materials* **2010**, *322*, 2375–2380, doi:10.1016/j.jmmm.2010.02.040.
50. Nowak-Jary, J.; Gronczewska, E.; Worobiec, W. Hampered Binding to Blood Serum Proteins and the Biological Activity of Antimicrobial Peptide Containing N3-(4-Methoxyfumaroyl)-L-2,3-Diaminopropanoic Acid Immobilized on Magnetic Nanoparticles. *Pharm Chem J* **2018**, *51*, 985–994, doi:10.1007/s11094-018-1728-2.
51. Sterzyńska, K.; Kaźmierczak, D.; Klejewski, A.; Świerczewska, M.; Wojtowicz, K.; Nowacka, M.; Brązert, J.; Nowicki, M.; Januchowski, R. Expression of Osteoblast-Specific Factor 2 (OSF-2, Periostin) Is Associated with Drug Resistance in Ovarian Cancer Cell Lines. *IJMS* **2019**, *20*, 3927, doi:10.3390/ijms20163927.